

DESIGN OF A NANOSCALE TIME-OF-FLIGHT SENSOR AND AN INTEGRATED
MULTISCALE MODULE FOR THE POINT-OF-CARE DIAGNOSIS OF STROKE

Matthew Andrus

A thesis submitted to the faculty at the University of North Carolina at Chapel Hill in
partial fulfillment of the requirements for the degree of Master of Science in the
Department of Biomedical Engineering.

Chapel Hill
2015

Approved By:

Steven A. Soper

Frances Ligler

Glenn Walker

Anne M. Taylor

© 2015
Matthew Andrus
ALL RIGHTS RESERVED

ABSTRACT

Matthew Andrus: Design of a Nanoscale Time-of-Flight Sensor and an Integrated Multiscale Module for the Point-of-Care Diagnosis of Stroke
(Under the direction of Steven A. Soper)

Stroke is a leading cause of death and disability in the United States, however, there remains no rapid diagnostic test for differentiating between ischemic and hemorrhagic stroke within the three-hour treatment window. Here we describe the design of a multiscale microfluidic module with an embedded time-of-flight nanosensor for the clinical diagnosis of stroke. The nanosensor described utilizes two synthetic pores in series, relying on resistive pulse sensing (RPS) to measure the passage of molecules through the time-of-flight tube. Once the nanosensor design was completed, a multiscale module to process patient samples and house the sensors was designed in a similar iterative process. This design utilized pillar arrays, called "pixels" to immobilize oligonucleotides from patient samples for ligase detection reactions (LDR) to be carried out. COMSOL simulations were performed to understand the operation and behavior of both the nanosensor and the modular chip once the designs were completed.

To my family and friends, without whom this endeavor would not have been possible. Thank you for your unwavering support.

TABLE OF CONTENTS

LIST OF FIGURES AND TABLES.....	vi
CHAPTER 1: INTRODUCTION.....	1
1.1 Diagnosis with Lab-On-A-Chip: Stroke.....	1
1.2 Single-Molecule Detection.....	3
1.3 Coulter Counter and Resistive Pulse Sensing.....	6
1.4 Thermoplastics in Microfluidic Applications.....	7
1.5 A Universal Molecular Processing System (uMPS).....	10
1.6 Structure of the Thesis.....	12
CHAPTER 2: A NANOSCALE TIME-OF-FLIGHT SENSOR.....	14
2.1 Sensor Description and Design Constraints.....	14
2.2 Resistive Pulse Sensing (RPS).....	18
2.3 COMSOL Assisted Iterative Design.....	19
2.4 Fabrication of a Nano Time-of-Flight Sensor.....	34
CHAPTER 3: INTEGRATED MULTISCALE MODULE FOR DIAGNOSTIC APPLICATIONS.....	38
3.1 Design Considerations and Requirements.....	38
3.2 Final Design.....	39
3.3 An Iterative Design Process.....	45
CHAPTER 4: CONCLUSIONS.....	50
REFERENCES.....	52

LIST OF FIGURES AND TABLES

Figure 1.1 – Example optical train.....	5
Figure 1.2 – Coulter counter patent drawing.....	6
Figure 2.1 – CAD drawing of nanosensor geometry.....	14
Figure 2.2 – Imported flight-tube geometry and electric field trace from COMSOL.....	22
Figure 2.3 – Initial 3D model with field strength shading.....	23
Figure 2.4 – Input funnel length experiment results.....	26
Table 2.1 – Results from the TBE buffer models.....	27
Figure 2.5 – Results from the particle size simulation.....	29
Figure 2.6 – Model for nanopore length simulations.....	30
Figure 2.7 – COMSOL results from the pore length experiments.....	31
Figure 2.8 – Blockage current traces for 20, 50, and 80 nm pores.....	33
Figure 2.9 – SEM image for nanochannel milled into silicon with FIB.....	35
Figure 2.10 – 3D AFM image of the 50 nm nanopore within the nanochannel.....	37
Figure 3.1 – Overview of the final chip design.....	40
Figure 3.2 – Steady state hydrodynamic flow profile through chip.....	41
Figure 3.3 – Hydrodynamic flow profile at critical regions.....	42
Figure 3.4 – Particle trace illustrating even distribution through chip.....	43
Figure 3.5 – Proportional arrow plot for electric field strength in chip	44
Figure 3.6– Electric field arrows at critical regions on chip.....	45
Figure 3.7 – Earliest design of multiscale module.....	46
Figure 3.8 – Image from heater simulation showing heater crosstalk.....	47
Figure 3.9 – Second generation design of multiscale module.....	48

Figure 3.10 – Close up images of final device with features labeled.....	49
--	----

CHAPTER 1

Introduction

1.1 Diagnosis with Lab-On-A-Chip: Stroke

Lab-on-a-chip (LOC) technologies can allow new diagnostic devices to reach patients in both the developed and the developing world in novel and powerful ways.¹ These devices can allow for highly sensitive, specific, and reproducible point of care tests with little more input needed from the user than the insertion of a patient sample. LOC devices possess a number of inherent advantages over traditional laboratory tests, including portability, low solution volumes, efficiency, and potentially cost.¹ These advantages make these devices especially well-suited for mobile applications such as emergency services vehicles.

Herein is described work towards a device for the rapid diagnosis of stroke in the pre-hospital setting. Technologies such as those that we are developing can be used in identifying and tracking genetic biomarkers that were previously too rare to detect and accurately measure over time with the existing diagnostic technologies. To generalize, this technology will allow for rapid and portable diagnoses utilizing very rare biomarkers.

A few facts and statistics will elucidate the importance of a new diagnostic technology for the rapid diagnosis of stroke. Stroke is a leading cause of death and disability in the United States and increasingly, around the world.² Unfortunately,

there are two variations of a stroke, ischemic and hemorrhagic, which are indistinguishable by current diagnostic methods such as computed tomography (CT) or magnetic resonance imaging (MRI). It is critical that the distinction made between these two disease states as quickly as possible because the treatments for ischemic and hemorrhagic stroke are very different and can actually be fatal if administered to a patient who has suffered the other type. The biggest example of this in assessing whether or not to administer tissue plasminogen activator (tPA), a treatment that is known to be very effective in ischemic stroke, yet is very dangerous and often fatal in hemorrhagic stroke. A rapid diagnosis could allow physicians to make the proper decision early in the treatment process. Additionally, there is only about a four hour treatment window available to stroke patients, lending to the common phrase “time is brain”.^{3,4} Rapid diagnostics will be critical to allow physicians to make the necessary diagnostic decisions within this pressing time window. Unfortunately, no reliable biomarkers have yet been discovered in the peripheral blood for indicating what type of stroke the patient has suffered. However, it has been demonstrated that mRNA can be harvested from specific white blood cells and a panel gene expressions can be utilized as a reliable biomarker for the diagnosis of stroke.^{5,6} Our system could allow for these mRNA panels to be quickly assessed in patient blood samples in a point-of-care setting. In a disease like stroke where getting the diagnosis correct very rapidly can save lives, this type of technology is extremely relevant.

1.2 Single-Molecule Detection

The goal of single-molecule detection (SMD) is to probe individual molecules in solution, gaining as much information about the molecule as possible. In addition, SMD can be used as a detection foundation in the clinic to detect very rare biomarkers and provide quantitative information with exquisite sensitivity due to the digital nature of the readout. The first detection of a single molecule occurred in 1989 by W.E. Moerner, who imaged a single pentacene molecule inside a solid crystal utilizing an absorbance measurement.⁷ A year later at Los Alamos National Laboratory, Shera *et al.* demonstrated the detection of single fluorescent molecules in solution.⁸ This successful experiment sparked a new area of research and many groups began working on and improving upon this technology for the accurate detection of single molecules in solution. Trautman *et al.* successfully imaged a single fluorophore on an air-dried surface in 1994 and Funatsu *et al.* imaged a single fluorophore attached to a protein molecule using total internal reflection fluorescence (TIRF) microscopy in 1995.^{9,10} This optical detection of a single molecule in fluid marked the birth of single molecule detection technologies. These technologies opened a new era in life sciences technologies, especially in the area of diagnostics. Biomolecules are now able to be individually probed, pulling important data out of previously averaged ensemble measurements.¹¹ This allows for the detection of much more scarce and specific biomarkers for diseases that would otherwise be extremely difficult to diagnose with traditional bulk measurements. In addition, SMD allows for the digital counting of single molecules that can provide

exquisite analytical sensitivity compared to analog measurements, which consist of bulk measurements.

Microfluidic systems have become a very popular platform for single molecule studies due to the ability physically isolate particles and utilize extremely low concentrations and low solvent volumes.^{12,13} Nanofluidics are even more attractive for SMD studies, as the benefits of microfluidics are further increased as the device dimensions continue to decrease. Moerner et al. has demonstrated that single molecules can be so confined in these nano-structures that Brownian motion is markedly decreased, allowing for more accurate observations.¹⁴

Traditionally, SMD schemes have relied on fluorescently tagging molecules to make them "visible" at specific wavelengths. This is an excellent strategy that allows for multiple channels to be monitored separately and simultaneously by utilizing multiple markers and excitation sources.¹⁵ Unfortunately, these types of systems require sophisticated and fragile optical trains that require precise alignment and calibration. While this type of system thrives in the lab, it can become useless once taken out into the field for point-of-care diagnostics. Figure 1.1 shows an example optical system utilized by our lab group; many of the components are made of glass and the alignments required for accurate measurements are on the scale of micrometers.

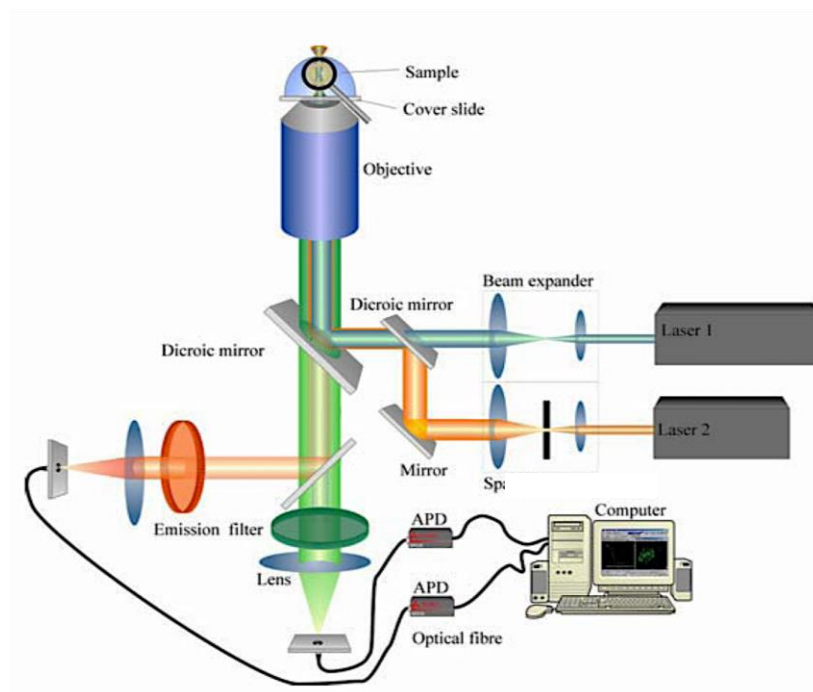


Figure 1.1 Example optical train for a SMD system. With many fragile components, including 532 nm and 650 nm lasers, and precise alignment required for accurate measurements; this type of system is not adapted to portable, rugged applications. (Designed by Zhiyong Peng)

Electronic detection modalities not only overcome this portability limitation, allowing SMD systems to be utilized in situations that would otherwise be unworkable, but also have advantages in both cost and miniaturization, making them much more scalable and commercially viable.^{16,17} Often, these electronic detection schemes involve nanowires or nanogap electrodes patterned into the fluidic substrate.^{18–21} However, there are challenges with the fabrication of electronic systems that can achieve single-molecule detection. Firstly, creating durable electrodes at the sizes required for a good signal to noise ratio is very challenging. Secondly, metal nanoelectrodes are very difficult to mate with thermoplastics, as they often delaminate within one use. While these nanogap

electrode strategies may work well in glass microfluidics, thermoplastic chips require different solutions for electrical detection of single molecules to be feasible.

1.3 Coulter Counter and Resistive Pulse Sensing

In 1949, Wallace H. Coulter patented his method for counting particles suspended in a fluid.²² This approach involved passing particles through an orifice with a current applied across the fluid. As the particle passes through the orifice, taking up volume, and displacing ions, the change in resistance across the device can be measured. The principle can be understood from one of Coulter's original patent drawings seen in Figure 1.2. Coulter originally created his technology for the US Navy during World War II, but its universal applicability was quickly realized and it was adapted to be utilized in many research and clinical applications.²³

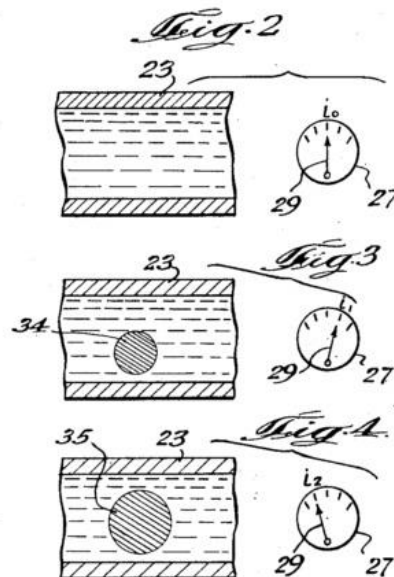


Figure 1.2 Original drawing from Dr. Coulter's 1949 patent showing the measured current through the constriction in three different scenarios (unblocked, blocked with more conductive particle, blocked with less conductive particle).²²

Cell counters that employed Coulter's technology allowed clinicians to rapidly and accurately count cells in clinical samples. Prior to Coulter's invention, blood cell counts were completed manually, wasting time and often yielding inaccurate and inconsistent results. This was simply the start of the Coulter counter's rise in clinical and research applications. Soon, Coulter's technology was being utilized in systems to count and size not only cells, but bacteria, prokaryotes, and viruses.²⁴

This technology has become the center of many clinical and diagnostic instruments, allowing for rapid, accurate particle counts in blood and other clinical samples. Much work has been completed in an effort to shrink this technology down to the microscale to allow for the counting of smaller particles with a decreased chance of co-residence errors.^{25,26} As this technology continues to shrink and the sensitivity of the electronics improve, Coulter counters are being used in more varied applications. Examples include the detection and counting of colloidal beads, pollen, metal ions, viruses, DNA, and antibody-antigen binding.^{24,25,27-33}

1.4 Thermoplastics in Microfluidic Applications

Traditionally, micro- and nanofluidic devices have been fabricated in fused silica or silicon, utilizing direct-write and chemical etching methods. These methods are often very expensive, time-consuming, and difficult to scale-up to commercial manufacturing processes. Increasingly, to address these shortcomings, polymer-based materials, particularly thermoplastics, are being utilized as an alternative in

the fabrication of micro- and nanofluidics. Thermoplastics are a class of polymers that exhibit softening behavior above their characteristic glass transition temperature while returning to their original state upon cooling. These polymers differ from elastomers and thermosets by their ability to remain chemically and dimensionally stable over a wide range of operational temperatures and pressures.³⁴

Typical thermoplastics utilized in fluidic applications include polycarbonate (PC), poly(methylmethacrylate) (PMMA), and cyclic olefin copolymer (COC); all of these polymers possess significantly lower glass transition temperatures (T_g) than that of glass, allowing for novel approaches to be used in the generation of nanostructures.³⁵ Typically, thermoplastics have excellent solvent compatibility compared to elastomers like PDMS, optical properties similar to glass, and the ability to be heated above their T_g and molded multiple times.^{36,37}

Our group typically utilizes modular systems, allowing for multiple materials to be used in the entire system, leveraging the advantages of each material while avoiding scenarios that would exploit their disadvantages.³⁸ In this way, each chip's material can be selected as the optimum substrate for the task that the chip was designed to carry out.

Polycarbonate is a low cost thermoplastic with several advantages. It has low moisture absorption, high impact resistance, a high glass transition temperature, and good transparency in the visible region of the electromagnetic spectrum. There are also several disadvantages of polycarbonate that must be addressed; namely poor solvent resistance to a range of organics and high

absorbance in the near UV and UV. Largely due to its low cost, polycarbonate remains a very popular microfluidic substrate in many applications, including chips for PCR reactions.³⁹

PMMA has a lower glass transition temperature, similar organic solubility, and similarly high absorbance in the ultraviolet (UV) range compared to polycarbonate. PMMA, although has a much lower fluorescence background compared to polycarbonate and better optical transmissivity in the near UV, making it more attractive for single molecule detection applications.⁴⁰ COC is often considered one of the most suitable thermoplastics for microfluidic applications due to a number of highly desirable properties. COC has a high glass transition temperature, good chemical properties, and optical properties that are even better than PMMA with their optical properties that approach that of glass in the UV-visible range. However, COC is not without drawbacks, as it exhibits very strong hydrophobic character that can degrade the performance of biological molecules without modification.⁴¹⁻⁴³

Another benefit thermoplastics possess over glass is the diversity of their surface chemistries' determined by the monomer units comprising the thermoplastic. Surfaces can be specifically selected for applications and can be modified or "activated" with oxygen containing functional groups by a number of simple procedures.⁴¹ Both UV and plasma activation have been verified as surface activation protocols capable of producing numerous oxygen containing groups including aldehydes, ketones, carboxylic acids, and alcohols.³⁷

1.5 A Universal Molecular Processing System (uMPS)

Microfluidic systems hold promise in creating diagnostic devices and protocols for disease detection and management that are difficult to monitor using traditional methods.^{1,44} These platforms allow us to probe RNA expression profiles of disease associated cells very rapidly and accurately to help guide decisions on how to treat that disease as well as diagnose that disease. Examples include probing circulating tumor cells (CTC's) to understand cancer progression or interrogating T-cells and neutrophils in patients that recently suffered a stroke to determine whether the stroke was ischemic or hemorrhagic.^{6,45-47} In clinical cases like these, a panel of biomarkers from the mRNA expression profile may be the only way to correctly diagnose and monitor the disease state in a timely manner so as to determine proper treatment.⁴⁸

Our group is developing mixed-scale systems (uMPS) engineered with a modular format in which task specific modules are integrated to a fluidic motherboard. By utilizing multiple scales we can mate the advantages of microfluidic processing domains with the inherent advantages of nanofluidic sensing domains.⁴⁹ In this type of platform, large blood volumes can be processed, allowing for a high probability of extremely rare biomarkers being found, which can then be subjected to downstream processing to elucidate the presence of the disease. These downstream measurements are made in nanofluidic domains, allowing for exquisite sensitivity and that take advantage of the unique physics adherent in this size domain. Thus, it becomes necessary to envision a sensing platform that can analyze milliliter sample volumes to search for rare biomarkers

from clinical samples and then, enrich these biomarkers into sub-picoliter volumes to accommodate the nanofluidic analysis.

In order to achieve this multi-scale operation, a hybrid driving mechanism was devised for manipulating molecules. Initially, all materials are moved onto the chip with hydrodynamic flow and all waste is removed in the same way. Then, when nano-scale measurements are to be made, the hydrodynamic flow is terminated and all materials are electrokinetically driven through nanoscale detectors. By utilizing discrete steps in this way, the microfluidic regions and nanofluidic regions can be in close proximity without disrupting the functionality of the other.

While there are a variety of different molecular markers that can be used to guide disease management scenarios, mRNA (messenger RNA) expression profiling is a common modality because it can provide information as to the activity of genes within the genome that are dysregulated in the diseased state.^{48,50,51} A common modality used for analyzing mRNA expression profiling is to use reverse transcription to convert the mRNA into cDNAs followed by a ligase detection reaction (LDR) to identify certain mRNA molecules via Watson-Crick base pairing.^{48,52,53} When measuring mRNA expression profiles using LDR, there is always a probability of a mis-ligation event causing a false-positive reading. Often this specificity error is simply accepted as inherent to the measurement and factored into the diagnostic decision-making process. The system that will serve as the anchoring technology for this thesis allows for the re-interrogation of ligation products in order to gain enough statistical power to remove these false-positives

entirely, allowing the specificity of the assay to approach 100%. This advantage will be further discussed along with more details about the system in Chapter 4.

To summarize, the work presented within this master's thesis is part of the development of the uMPS that can select circulating markers (cells or exosomes in this example) for *in vitro* diagnostics to manage several different diseases. The modular design approach offers many unique advantages compared to a monolithic one such as: (i) Using materials and manufacturing techniques appropriate for a particular application; (ii) generating a toolbox composed of functional modules that can be mix and matched for a variety of assays; and (iii) the ability to process a sample across a large volume range (mL \rightarrow fL) and efficiently analyze rare targets at the single-molecule level.

1.6 Structure of the Thesis

This thesis discusses in detail the design and simulation results of the multi-scale fluidic device for sensing single molecules serving as markers for certain disease states. The thesis will elaborate on the design, modeling, and fabrication of the time-of-flight nanosensor and its ancillary components.

The first chapter introduces the background on this project and gives a general overview of the work that was completed. Additionally, many of the important principles and physics underlying this work are introduced and discussed, including single molecule detection (SMD) technologies, resistive pulse sensing (RPS), and the use of thermoplastics and microfluidic and nanofluidic

devices. At the end of this chapter is a brief summary of the structure for the remainder of the thesis.

The second chapter focuses on the nanoscale time-of-flight sensor. It describes the design considerations, finite element analysis, and fabrication of this device. This chapter will highlight some of the challenges in working with nanoscale structures as well as some of the future techniques that will be deployed to overcome these difficulties.

The third chapter will discuss the design and simulation of the multiscale module for use in diagnostics. This chapter will also detail how this device will be further developed and utilized in certain disease states in conjunction with different collaborators. In the future, this device will be part of a universal molecular processing system (μ MPS) for the comprehensive molecular analysis of cellular and molecular markers isolated from clinical samples that will be briefly introduced to further frame the work done in this master's project.

The fourth chapter will briefly summarize the work that was done in this master's project. Some concluding thoughts and remarks will be included as well.

CHAPTER 2

A Nanoscale Time-of-Flight Sensor

2.1 Sensor Description and Design Constraints

The sensor utilized by the multiscale platform discussed in this thesis consists of a nanoscale time-of-flight (TOF) sensor. The basic structure of the sensor can be seen in Figure 2.1.

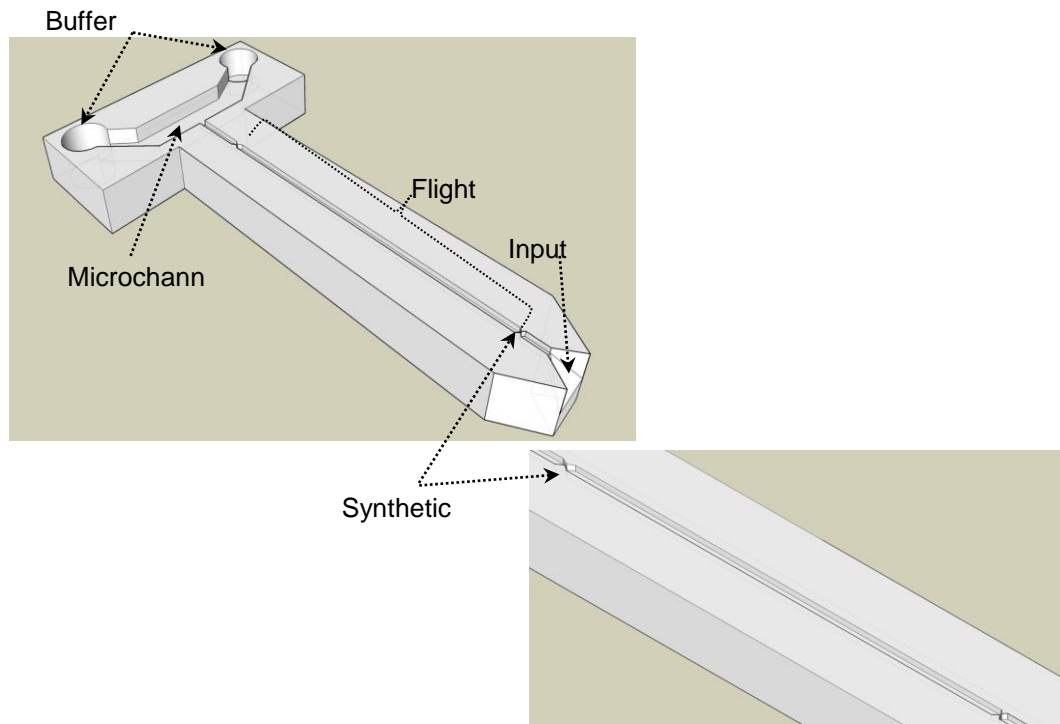


Figure 2.1 Computer assisted design image of the basic sensor geometry with important structures labeled.

By fabricating a nanochannel with two nanopores embedded within it, we can make time-of-flight measurements that allow us to interrogate and identify molecular entities flowing through the nanochannel; the time-of-flight provides a molecular identification due to the unique electrophoretic mobility of the particular entity within a nanochannel. The key to implementing this identification modality is to use a simple and robust technique to measure the mobility as a single molecule electrophoretically travels through the flight tube. In this case, we will discuss the use of in-plane synthetic nanopores positioned at the input and output ends of the nanometer-scale flight tube that generates a resistive pulse due to carrier buffer ion exclusion when the target molecule travels through the pores. Thus, the mobility is measured from the known electric field strength and distance between the pores as well as the measured time of travel between the pores.

The pores are essentially coulter counters placed in series, giving a signal at each pore as well as a time-of-flight measurement as the molecule travels the fixed distance between the two pores. By utilizing an electrical method for detection, we are able to simplify the auxiliary hardware needed to run the system and also, negate the need for labeling the molecule we are interrogating; a molecular label can perturb the electrophoretic mobility of the target molecule.

The sensor will be placed at the end of our universal molecular processing units (uMPS), creating the readout for the single molecules of interest. These molecules will vary in size depending on the sample being analyzed and the upstream processing steps performed. As was discussed previously, we need a sensor that can resolve single stranded DNA (ssDNA) molecules of length 40-100

nucleotides that act as diagnostic biomarkers in stroke, cancer and other disease states of interest. In most cases, these biomarkers will be labeled oligonucleotides produced from our solid phase ligase detection reactions upstream of the sensor. In order to provide measurements on the order of single molecules in a thermoplastic micro-/nanofluidic chip with the sensitivity to identify distinct single molecular species, a sensor had to be designed that utilized resistive pulse sensing technology (the Coulter principle). As was previously discussed, resistive pulse technology was selected as the modality for this application because of the ability to make these structures in thermoplastics with high reproducibility and scalability. Additionally, the external equipment (electronic components) required to drive and readout from these sensors are much smaller than those required for optical systems.

It was decided that a time-of-flight sensor with two RPS regions separated by a nano flight tube would be the basis for the nano-sensor for our systems. This builds on work that has demonstrated the use of nanopores in the detection of single molecules. The decision to use a time-of-flight type measurement gives the user three useful data points with each particle measurement. One current pulse when the particle passes through the first pore, a second pulse when it passes through the second, and the time-of-flight information from the duration between the two pulses. These three data points will allow for the ability to accurately determine the identity of the molecule passing through the time of flight tube. Additionally, this sensor must be easily fabricated in the same embossing step as the rest of the chip geometry to make the production of such chips scalable. This means that the structure needs to be something that is possible to fabricate utilizing a focused

ion beam milling process and nano-imprint lithography (NIL). Structures too complicated or small for these processes would change our fabrication strategy and increase the time and cost required to fabricate each device.

The first variables that were considered were simply those involving the size of the nanochannel containing the time of flight sensor as well as the dimensions' of the features contained within this region. Perhaps the most important thing to consider when thinking about this nanochannel in terms of resolution is the overall length of the gap between the two nanopores. It was determined that a 100 micron total channel length with 80 microns between the two pores should be a sufficient starting dimension to achieve acceptable resolution of the single molecules passing through the flight tube. This was decided based on average particle sizes that might be seen in this sensor as well as the nano-electrophoresis studies done by other members of the lab. A time-of-flight length of 80 microns will allow particles of various sizes to be driven at a range of different voltages while still residing within the flight tube long enough to distinguish between the two pulses. Another very important consideration when designing this sensor was the possibility of co-residence of molecules within the flight-tube. Co-residence will not be a large issue with the type of diagnostic applications we are interested in, as the biomarker populations are so small, however, it is still worth designing out of the system as much as possible. Several strategies can be utilized to mitigate the risk of co-residence occurring and fouling the data. The first is creating sufficiently small channels where the physical probability of co-residence is sufficiently diminished. The second is creating slightly different geometries for the two pores so that the

initial “entry” pulse can be distinguished with 100% confidence from the second “exit” pulse. The simplest example of this would be making the second constriction 2-3 times as long as the first. This would significantly alter the shape of the waveform created by the molecule passing through the pore so that it would be easily distinguished from the first pore’s signal. Understanding that all of these variables can be easily adjusted to fit specific tasks utilizing certain molecular species makes this a very powerful and adaptable sensor design.

2.2 Resistive Pulse Sensing (RPS)

Many applications require the direct counting of particles on the microscopic scale. For decades, the Coulter counter has been utilized as a device to perform this functionality automatically and rapidly for particles suspended in an electrolyte solution.²⁴ As particles pass through a constriction, electrolytes are pushed out of the volume, altering the resistance within the channel. This change is measurable, directly related to the resistivity of the particle passing through the channel, allowing for accurate counting and limited identification capabilities. To understand these events we can look at Equation 1 (DeBlois and Bean) which describes the resistive effects of a particle that is much smaller than the surrounding channel, which is a good approximation for most applications. Equation 1 is given as:

$$\Delta R = R_2 - R_1 = \rho d^3 / \pi D^4$$

where R_2 is the resistance of pore with the particle inside it, R_1 is the empty pore, ρ is the resistivity of the particle, d is the diameter of the particle, and D is the diameter of the pore. The change in resistance is proportional to the cube of the diameter and inversely proportional to the fourth power of the pore diameter for most applications.²⁴ Additionally, some specific analytes require geometry adjustments to better suit the actual physics occurring within the pore geometry. For example a recent paper out of the Jacobson group describes the use of resistive pulse technology for the discrimination of T=3 and T=4 HBV virus capsids. In order to mathematically describe these capsids, the particle is treated as a porous spherical shell, or a hollow “wiffle ball” geometry, filled with electrolyte.⁵⁴ In the case of the polystyrene bead experiments, such alterations may be necessary if the simplified equations do not correspond well with experimental values. For ssDNA measurements a “polymer chain” type geometry where multiple spheres pass through the pore in series may be the best way to approximate the behavior and physics of the oligonucleotide markers in solution.

2.3 COMSOL Assisted Iterative Design

In working to develop a nanoscale time of flight sensor for the universal molecular processing unit, an iterative design process was utilized in tandem with COMSOL simulations to refine the geometry at each step. By utilizing two nanopores in series in a nanochannel, we are able to harness the coulter principle and make a time of flight measurement as a particle passes between the pores. This strategy has been utilized to detect single molecules on the nanoscale in a glass

device, indicating that this strategy will be successful in thermoplastics with even smaller channels and particles.⁵⁴ Our device doesn't need to achieve mononucleotide resolution, but small oligonucleotide products will be the targets identified in this sensor. This will eventually require structures on the order of 1-10 nanometers. However, it would be impractical to immediately begin by trying to design and fabricate a microfluidic with structures on the order of only a few nanometers. Accordingly, it was decided that a proof-of concept device with larger dimensions (about 10X larger than the desired dimensions for the final device) would be the ideal beginning step for this project.

Initially a two-dimensional single nanopore was created within a nanochannel with the aid of computer assisted design software (AutoCAD 2014). This 2D pore essentially assumes an infinitely flat circle with the same properties at the particle moving through an infinitely flat channel with the same properties as the three-dimensional fluidic channel. This single pore was then imported into COMSOL Multiphysics 4.3 and utilized as a basic model to look at the behavior of the electric field around the nanopore structure. This basic structure was then extrapolated into a two-dimensional time-of-flight nanochannel with the two nanopores separated by 100 micrometers. The nanochannel had a width of 100 nm and the pores constricted to 50 nm. Additionally, an input funnel was included, as previous work from Dr. Soper's lab group had shown that input structures allowed more particles to migrate into the nanochannel.⁵⁵ An electric field was created using a 10 volt driving potential from before the input funnel to the output fluidic reservoir. This electrical connection was meant to mimic how the current would

flow through the nano flight tube when it is embedded into a universal molecular processing chip; that is to say, it will not be an isolated entity. Figure 2.2 shows the imported nano flight tube geometry and the resulting electric field trace. This simulation is very different from most of the others, as it had no flow considerations. The voltage was simply applied to a conductive two-dimensional channel surrounded by an insulating wall.

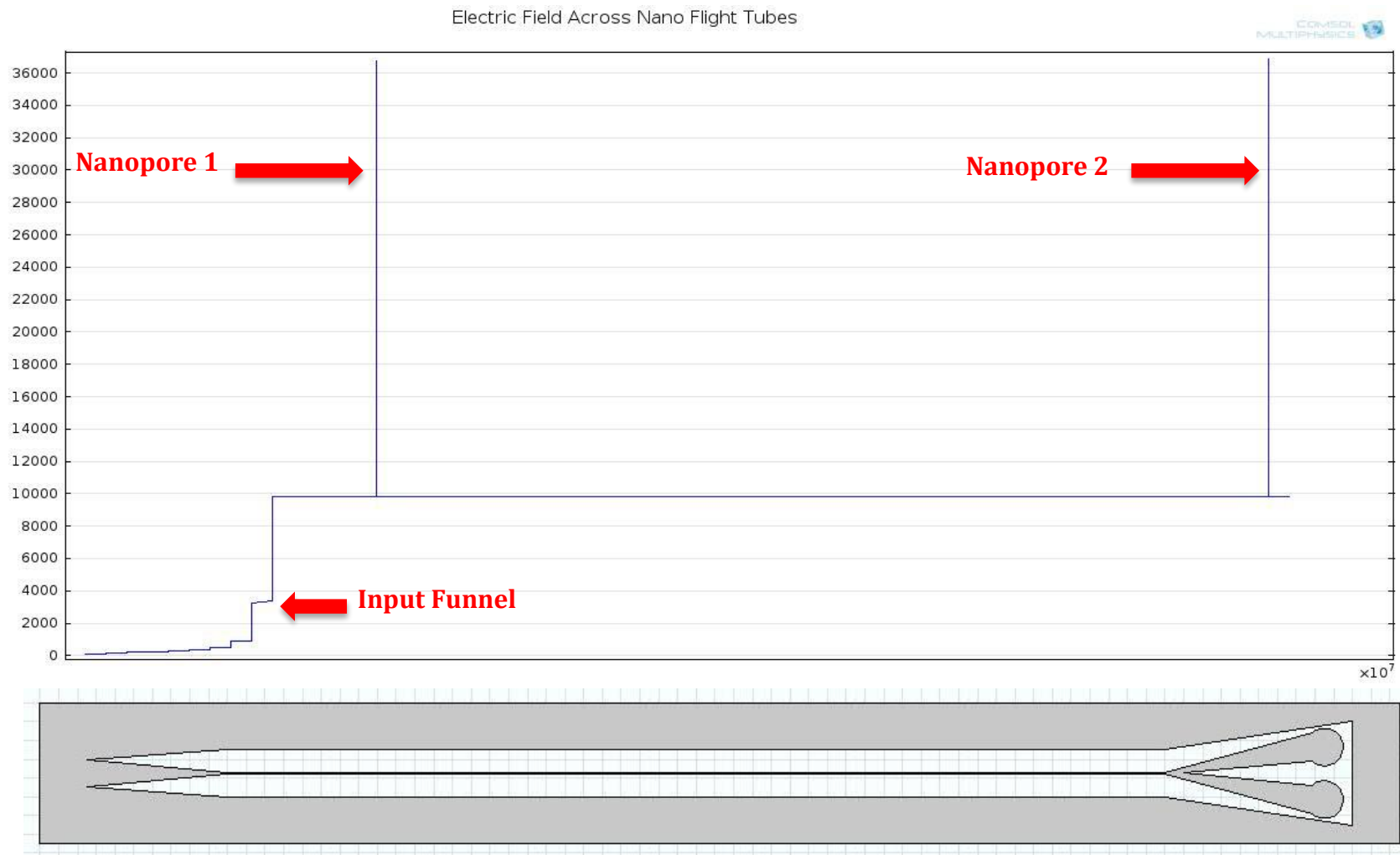


Figure 2.2 Two-dimensional flight tube imported into COMSOL with electric field trace resulting from 10 V potential applied through the center of the channel. This simulation was performed with a fine mesh and channel resistance with water.

A two dimensional model quickly became insufficient to understand the properties of a true three-dimensional nanopores and not just a channel constriction in one dimension. Again, initially a system with an input funnel and a single nanopore was created for simplicity and simulation processing time. By comparing the initial results from this model to that of the two-dimensional model containing two pores, we found that this model could be accurately extrapolated into a two-nanopore flight tube. This model had a nanochannel with a 100 nm X 100 nm cross section and a 50 nm X 50 nm X 50 nm pore (Figure 2.3).

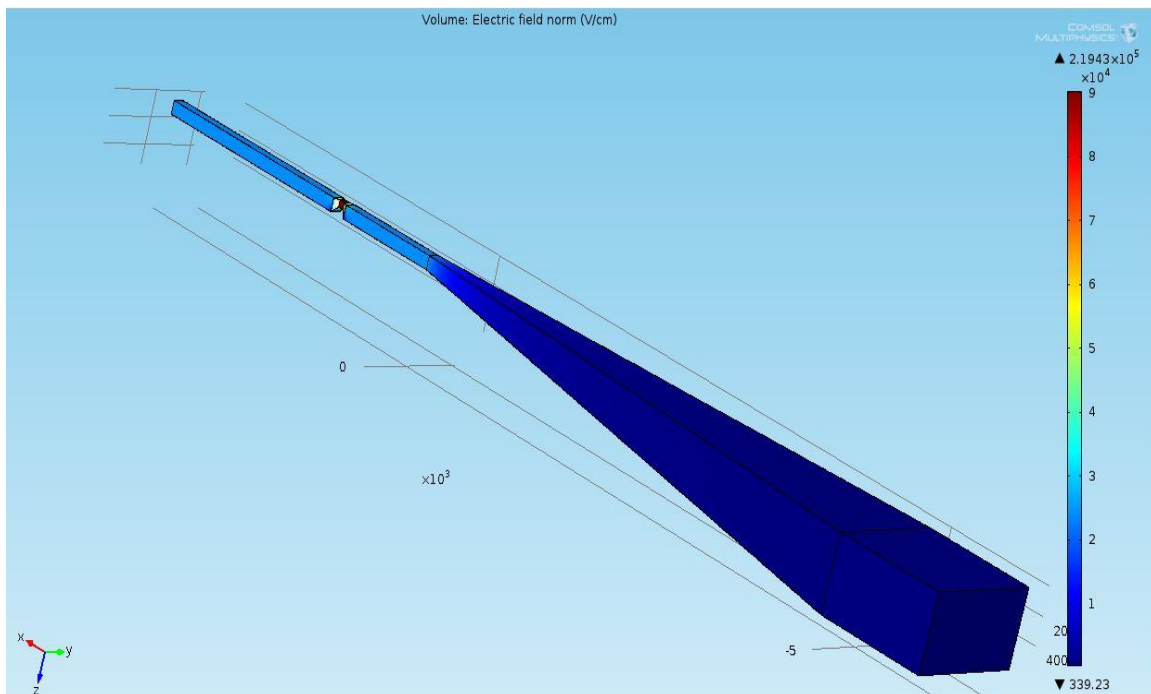


Figure 2.3 Initial three dimensional model with 50 nm pore and input funnel; a 10 V potential was applied and the color chart represents the resulting electric field strength.

This 50 nm pore was designed to be utilized with simulated 40 nm polystyrene beads, which would act as an example particle for the larger-scale proof of concept

system. This model relies on the Coulter principle, or a resistive pulse measurement, as it is more commonly named to in the literature. The current blocking measurement is dependent upon how many ions the insulating particle (polystyrene bead) can displace within the detecting volume (the nanopore). In the case of this model, the 40 nm polystyrene bead displaces 33.5 zL of the 125 zL detection volume. This is approaching an idealized situation, where the particle takes up as much space in the detection volume as possible without risk of physical blockage. Considering actual polystyrene nanobeads typically have a tolerance of $\pm 10\%$ and nanochannel walls created by FIB milling often have a slope induced by the Gaussian profile of a focused ion beam, this is the tightest fit that we could confidently model. This yields a volume displacement of approximately 27%. Fortunately, the volume displacement in the current blocking measurement isn't the only critical variable, the ionic strength of the buffer and the applied potential affect the duration and magnitude of the signal generated by a particle passing through the detection volume. These variables will have to be fine-tuned depending on what size particles are being passed through the actual device and what their electrical properties are.

The first variable assessed with this model was the length of the input funnel. Previous research has demonstrated that the geometry at the input of the channel affected the rate at which particles enter the channel.⁵⁵ However, we were also interested in the effect the geometry has on the electric field, particularly across the nanopore. This was investigated by keeping the overall length of the channel and funnel constant along with the applied voltage while varying the length of the funnel

from 1 micron to 11 microns. Additionally, the boundary dimensions were held constant: in all trials, the funnel sloped from a channel with dimensions of $2\text{ }\mu\text{m} \times 1\text{ }\mu\text{m}$ to a channel with dimensions of $100\text{ nm} \times 100\text{ nm}$. The results from this experiment can be seen in Figure 2.4, along with a close up view of the electric field at the nanopore (indicating a lack of dead volume). A number of interesting findings came from this experiment:

- 1) The funnel length drastically affects the slope of the electric field at the transition region from the funnel to the nanochannel. The longer the funnel, the less severe the rise in electric field strength. This will not only affect the number of particles entering the nanochannel but also the rate at which particles are entering the sensor.
- 2) The longer the input funnel, the lower the electric field strength at the nanopore. This is very important when considering how rapidly a particle will move through the detection region and the ability of the electronics to capture this event (sampling frequency limitations).

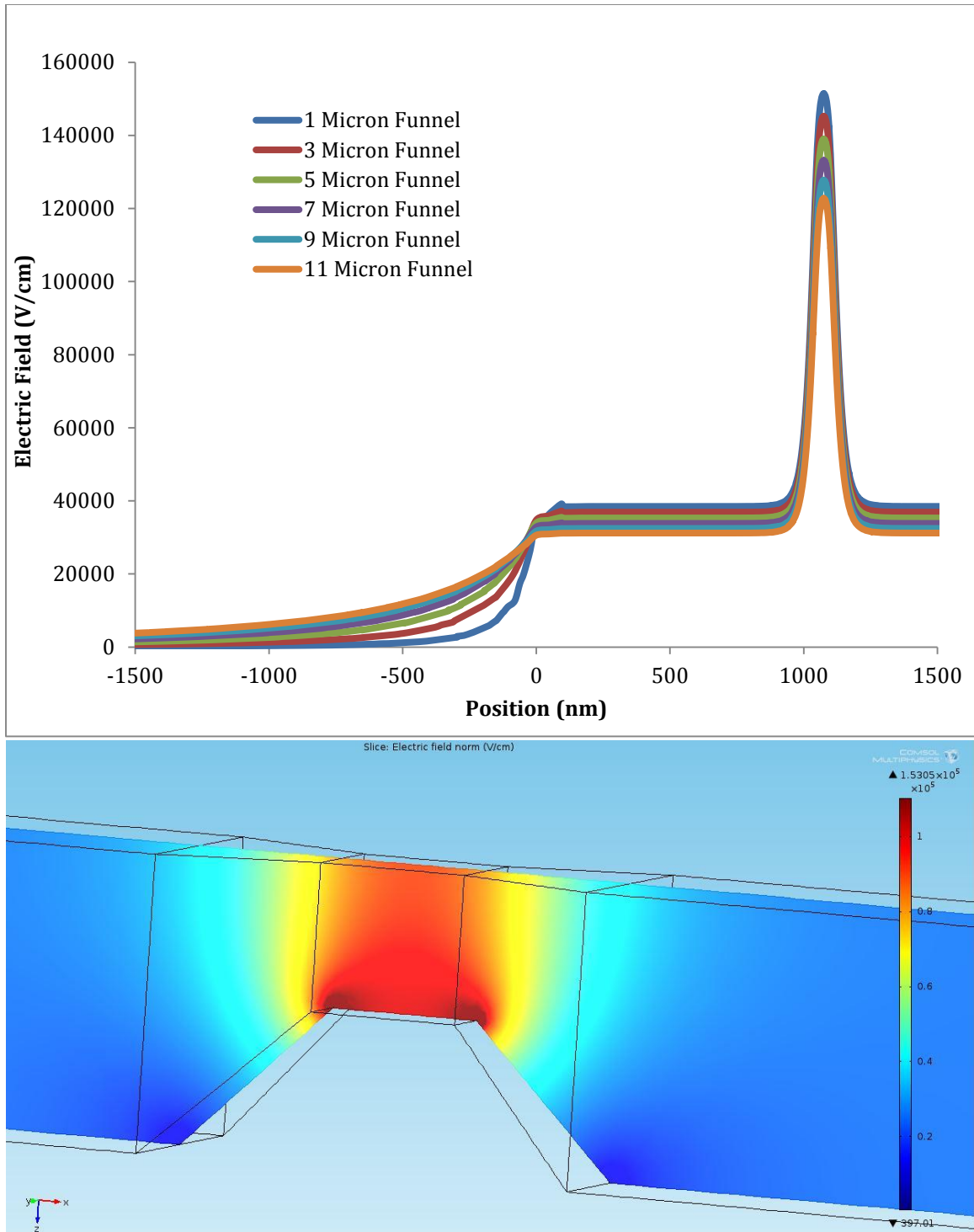


Figure 2.4 Graph displaying results from input funnel length experiment in which the input funnel was varied from 1-11 μm and the channel size was held constant at 100 μm X 100 μm . A close-up of electric field at the nanopore is also provided to show the sharp rise seen on the graph.

The next experiment performed utilizing this model was a buffer concentration experiment to understand how the buffer would affect not only the baseline current recorded but also the change in current as a particle passed through the detection nanopore. Tris-borate-EDTA (TBE) buffer was selected as the buffer because of its prevalence in electrophoresis experiments, particularly those involving nucleic acids. For this experiment the funnel length (10 microns), driving potential (10 V), and pore geometry were all held constant. The TBE buffer concentration was varied from 1.0X to 2.5X. The measurement was taken from the simulation as the particle was in 11 different positions, but essentially we can think of two conditions: a blocked condition, where the particle is centered in the detection nanopore, and an unblocked condition, where the particle is in the larger channel on either side of the nanopore. Table 2.1 shows the summarized results from the modeled buffer experiment.

TBE Concentration	Conductivity (S/m)	Empty Current (nA)	Blocked Current (nA)	Difference (nA)	Percent Difference
0.5X	0.576	19.17	18.53	0.64	3.35%
1.0X	0.901	29.98	28.98	1.00	3.35%
1.5X	1.083	36.04	34.83	1.21	3.35%
2.0X	1.389	46.22	44.68	1.55	3.35%
2.5X	1.700	56.57	54.68	1.89	3.35%

Table 2.1 Results from the TBE buffer models.

The TBE buffer experiment indicated that the TBE buffer concentration not only changes the baseline current through the nano flight tube proportionally to the conductivity of the buffer, but the current change when the pore is blocked is also changed by this scale factor. This means that the highest buffer concentration feasible in a physical device will give the highest amplitude signal at each nanopore.

The final experiment performed utilizing this model was a study on the effect of the particle size on the sensor response. This was a critical experiment for understanding how the sensor would perform in a real setting where different analyte molecules of varying sizes will be flowing through the sensor in one run. Going back to the physics of the Coulter counter, this is very important because the size of the particle determines how much conductive volume is being displaced. This can be done through an experiment with two measurements, one in the unblocked state and the other in the fully blocked state. The input funnel length, buffer concentration, driving potential, and the sensor geometry were all held constant for this simulation. The particle remained a sphere and always passed directly through the center of the detection volume, but the radius of the sphere was varied from 15 nm to 24 nm. This is not a practical experiment for a physical device because of the variance in the polystyrene nanobeads; a COMSOL simulation is an excellent way to understand the response of the sensor without risking blockage of a test device. The sensor's blockage current value exhibited a nonlinear response to the particle diameter and the proportion of the detection volume blocked by the particle. As would be expected, the greater the diameter of the particle, the greater the magnitude of the current drop when the particle resided in the nanopore

detection volume, as was stated previously. However, the increase was not linear, but rather exponential as the blocked volume approached the total detection volume of the nanopore. This behavior indicates that great care must be taken when deciding upon the dimensions required for a specific application. Too large of a pore and some smaller analytes may go undetected, too small of a pore and larger molecules could potentially block the sensor. The results of this experiment can be seen in Figure 2.5.

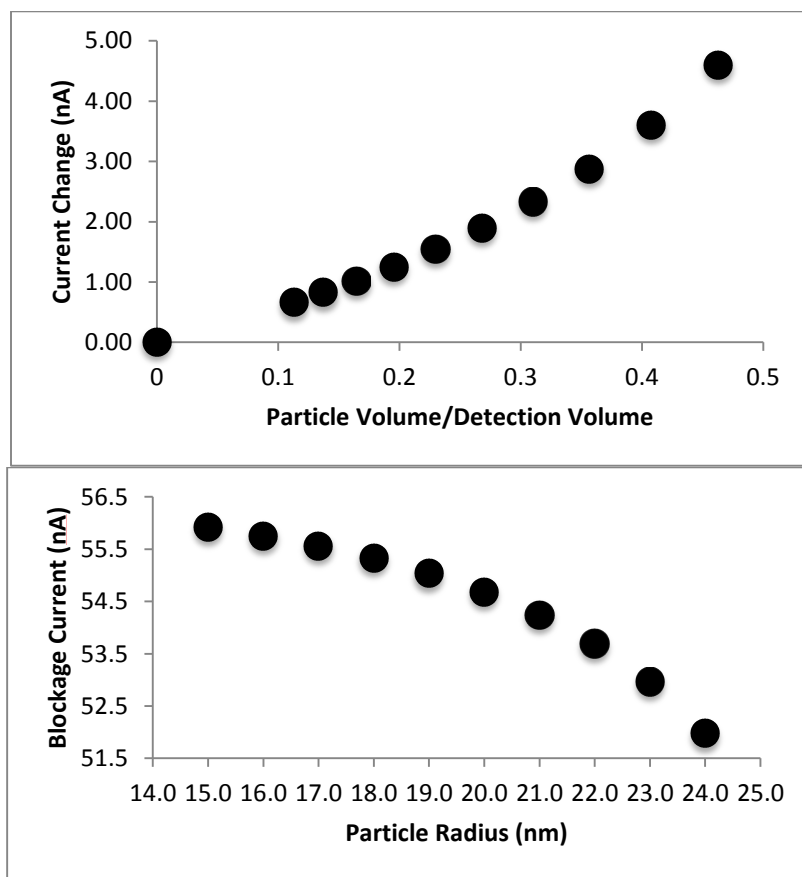


Figure 2.5 Results from the particle size simulation represented in two graphs. The first examines the overall blocked current vs. particle radius, the second shows the current drop vs. the proportion of the detection volume filled by the particle. The sphere's diameter was varied from 30 nm to 48 nm within a 50 nm X 50 nm X 50 nm pore geometry. TBE buffer was utilized as well as a 10 V driving potential.

The final simulation utilized a new model with only a nanochannel and a nanopore centered within it. Removing the input funnel and other extraneous volumes allowed for faster simulation processing time as well as enhanced signal measurements from the model with a much finer mesh. Again this model was initially designed in AutoCAD 2014 and then imported into COMSOL 4.3; it can be seen in Figure 2.6.

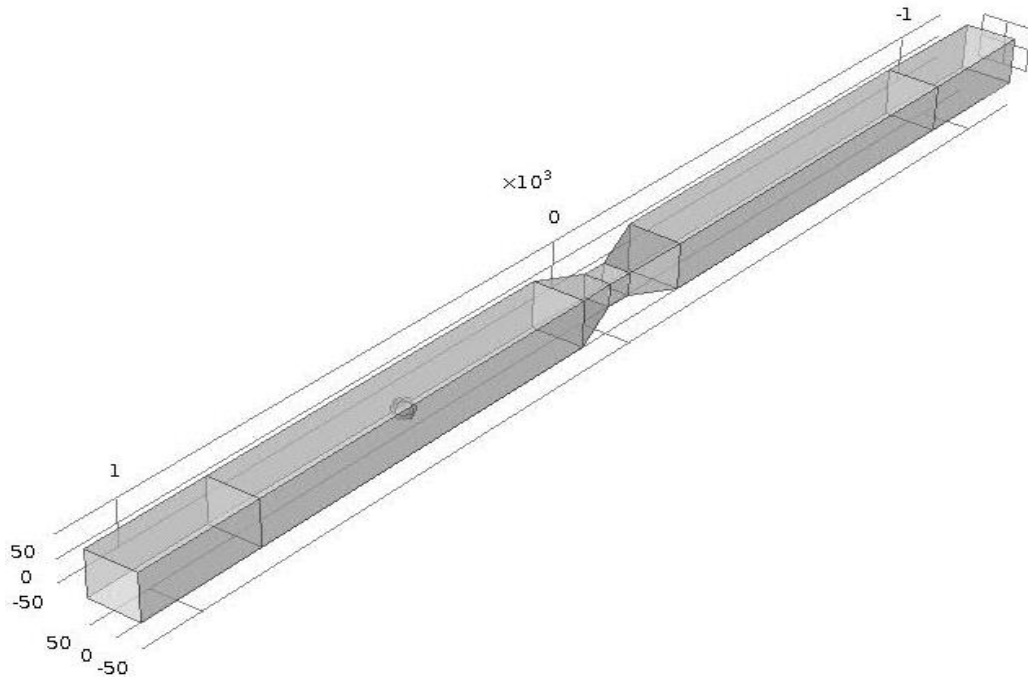


Figure 2.6 Model for nanopore length simulations in which finer meshes were used to further understand the behavior of the particles and their signals as they passed through the pore.

The polystyrene bead can be seen in the first part of the nanochannel before the pore. This bead was “stepped” through the nano flight tube and current measurements were taken at 45 distinct points. This process was initially repeated for pore lengths ranging from 10 nm to 80 nm. For these experiments the other

channel dimensions as well as the radius of the polystyrene sphere (20 nm) were held constant, along with the buffer concentration (2.5X TBE) and driving potential (10 V). It was found that the pore lengths closest to the particle diameter displayed the largest current drop. Additionally, it was found that longer pores produce longer signals, whereas shorter pores produce shorter signals. These results can be seen in Figure 2.7.

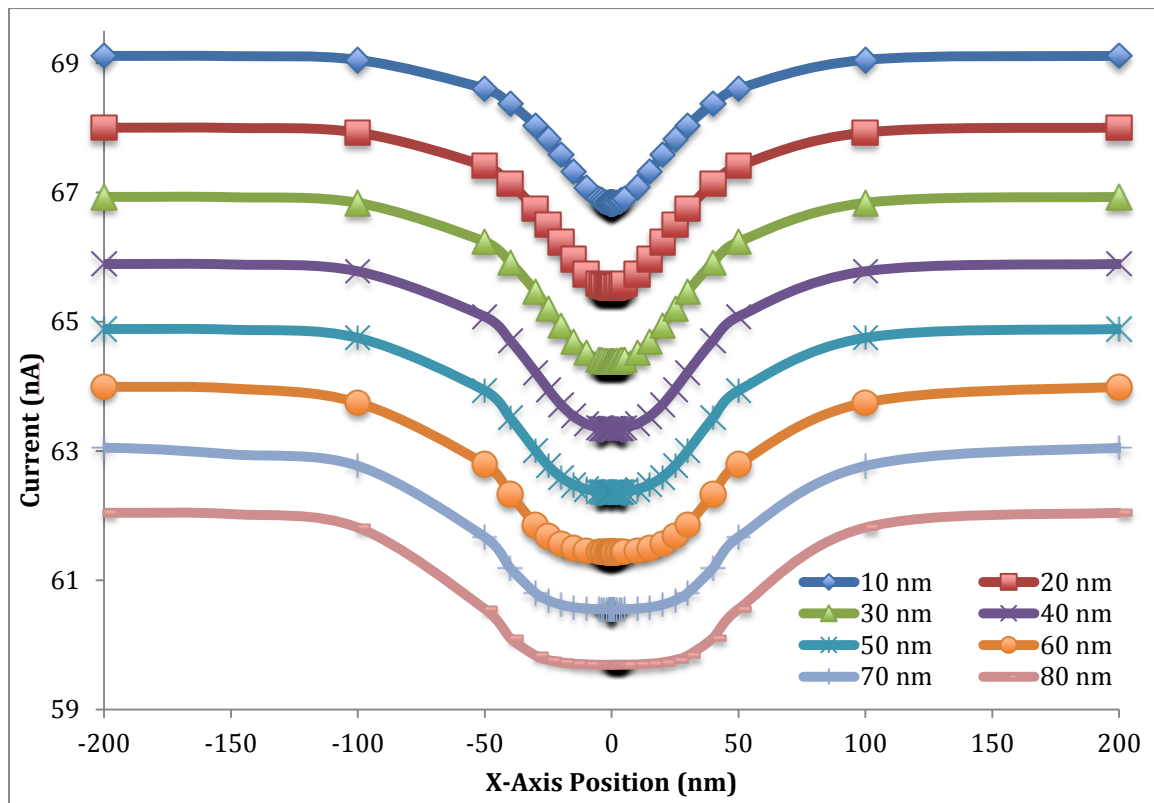


Figure 2.7 Simulation (COMSOL) results showing the effects of pore length on the current response generated. A pore with a cross section of 50 nm X 50 nm was varied in length from 10 nm to 80 nm. For each length a polystyrene bead with a diameter of 40 nm was stepped through positions inside of the pore, the resultant drop in current was recorded.

After obtaining data from this initial pore length experiment, we wanted to refine the model further to better understand the relationship between the pore length and the shape of the signal output from the sensor. The same geometry as shown in Figure 2.6 was used but with a finer mesh, especially around the curvature of the polystyrene sphere. Again, it was demonstrated that the lengths closest to the diameter of the particle showed the largest current drop, with diminishing signals as the pore length got much larger or smaller, as shown in Figure 2.8. The difference in the width of the signal was also seen more clearly, further elucidating the idea that the sensor geometry could be modified to match the hardware that is performing the current measurements. For systems where the sampling frequency limit is being approached, a longer pore could allow for more particles to be correctly detected. Conversely, for systems where the dynamic range is the limiting variable, a shorter pore, closer to the diameter of the particle, could be used to ensure that the signal has the highest amplitude possible. This experiment further aided in our understanding of the adaptability of this sensor design and the way it can be manipulated to ensure optimal data collection in a physical device.

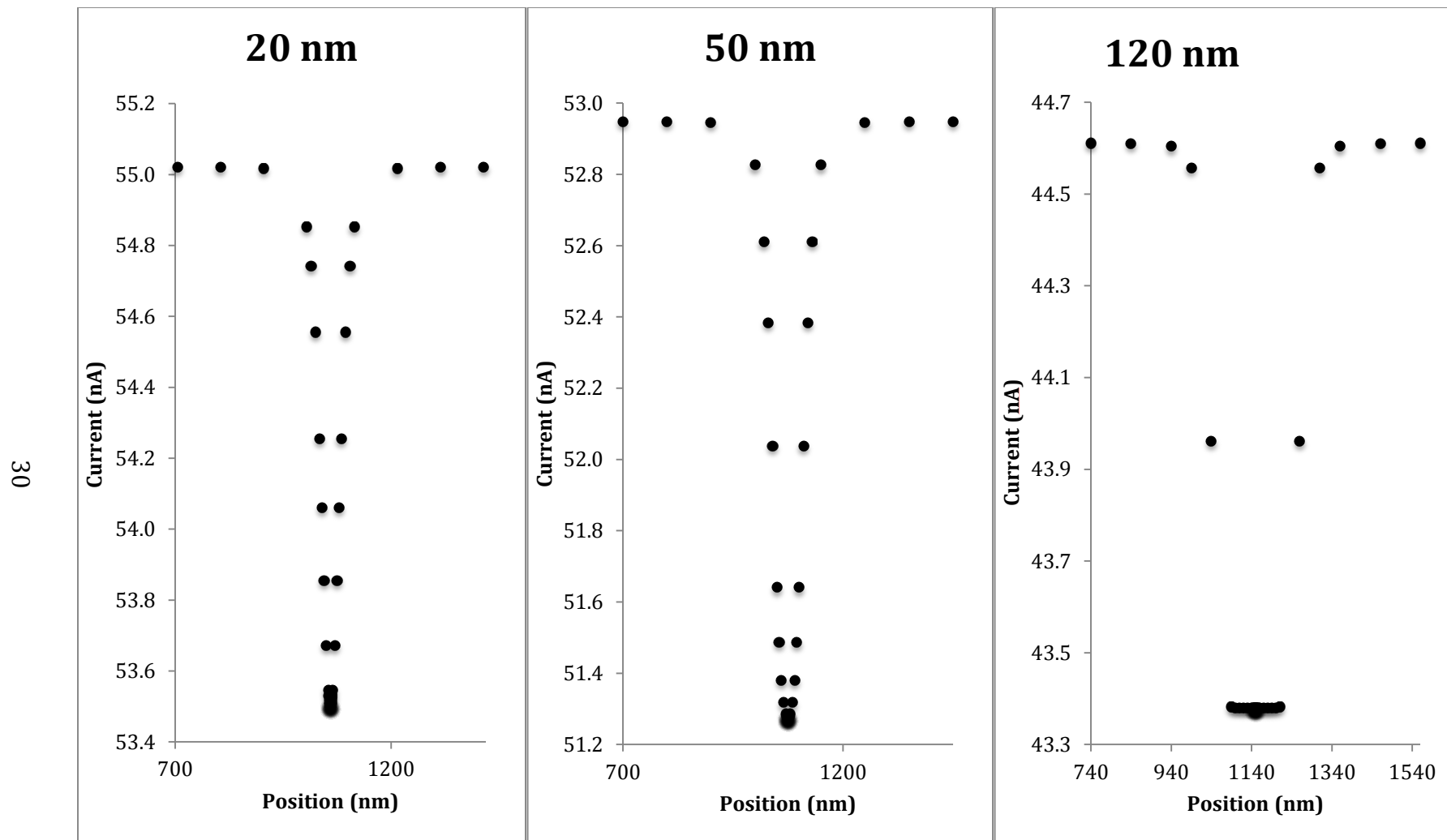


Figure 2.8 Blockage current traces for simulations with 20, 50, and 120 nm detection pore lengths. The 20 nm pore recorded a current change of 1.52 nA, the 50 nm pore recorded 1.67 nA, and the 120 nm pore recorded 1.23 nA.

2.4 Fabrication of a Nano Time-of-Design Flight Sensor

Once the sensor geometry had been modeled and the variables affecting the current blockage signal were better understood, it was time to begin fabrication of a nano flight tube. We utilized a nanofabrication method that has been reported in the literature.^{55,56} The first step in this process involved creating the microstructures that serve as reservoirs and feed channels in a pure silicon wafer. Two v-shaped access channels were patterned into a standard silicon <100> wafer (University Wafers, Boston, MA) utilizing standard photolithography and anisotropic etching with 50% KOH. These channels measured 55 μm wide by 12 μm deep, and 1.5 cm long. All of this was completed in the UNC clean room.

The next step in this process was calibrating the input variables to the output structures on the focused ion beam (FIB) (FEI Helios 600 Nanolab DualBeam System). By milling structures and then analyzing and measuring them, we were able to create a “calibration curve” for the channels milled by the FIB. At the same time, 24-bit gradient bitmap files were created, which contained the desired structures to be milled into the silicon wafer. A number of strategies were attempted to achieve the optimal result. Finally, it was decided upon that the entire nano flight tube would be milled in one ion exposure with the guidance of one gradient bitmap image. This produced the most consistent results, minimized the exposure of the silicon to ion and electron bombardment, and reduced the risk of drift causing misalignment of structures. The final device was produced with a milling current of 9.7 pA, a dwell time of 1 μs , and a mill time of 5:24. The resulting

structure successfully connected the two access microchannels and produced all of the features from the bitmap, shown in Figure 2.9.

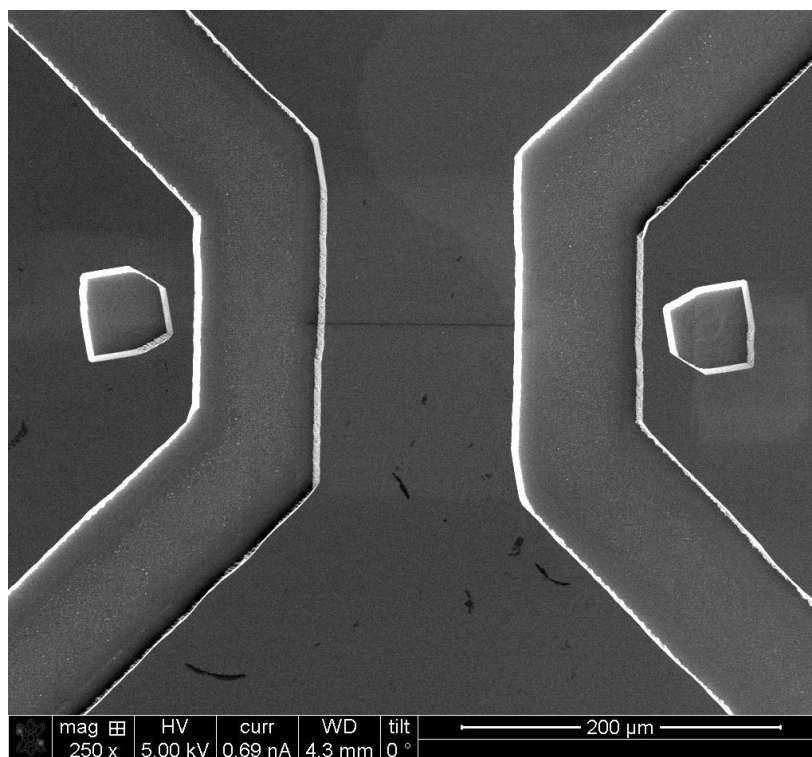


Figure 2.9 Zoomed out SEM of nano flight tube between access microchannels in a silicon wafer. The microchannels were produced with anisotropic wet etching techniques and the nanochannel was produced via FIB milling with a milling current of 9.7 pA, a dwell time of 1 μ s, and a mill time of 5:24. (FEI Helios 600 Nanolab DualBeam System)

The next fabrication step involved the production of a resin stamp from the silicon master so that the structures that have negative tone on the master can have positive tone and be imprinted into thermoplastics. This is accomplished by first silanizing the silicon master in a desiccator for 3 hours. A drop of a UV-curable resin mixture (68 wt% tripropylene glycol acrylate (TPGA), 28 wt% trimethylphenylammonium (TPMA), and 4 wt% Irgacure 651) was then placed on

the surface of the silicon master and lightly pressed down with a scored piece of 6017 COC (Topas Advanced Polymers, Florence, KY) to serve as the backplate of the stamp. Once all bubbles were removed and the resin had completely filled the structures on the silicon master, the entire assembly was placed into a CL-100 Ultraviolet source and exposed to 365 nm (10 J/m^2) UV light for 6 minutes to ensure complete crosslinking of the resin and adhesion to the COC backplate. The assembly was then removed and the now cured stamp was carefully demolded from the silicon master.

Next, the structures in the stamp were or imprinted into a 1.5 mm thick PMMA (Good Fellow, Berwyn, PA) substrate that would be the final chip containing the nanochannel and nanopore. Imprinting was performed using a HEX03 from JenOptik with a pressure of 1910 kN/m^2 for 120 seconds. During the imprinting step, the top and bottom platens were held at a temperature of 125°C . Once the imprinting step was complete, the platens were cooled to 40°C and the pressure was removed. The PMMA chip was then carefully demolded from the resin stamp and four holes were drilled, one at each reservoir. After the holes were drilled and all debris was removed from the chip, the PMMA substrate and a 8007 COC cover plate were oxygen plasma treated for 2 minutes to clean the surfaces and decrease their water contact angle. The substrate and cover plate were then pressed together and sealed in an airtight vacuum bag to begin the bonding. The assembly was then removed from the bag and placed between polyimide films and rubber sheets, and then placed in the HEX03. Once the chamber closed, both platens were brought to 70°C and a pressure of 660 kN/m^2 was applied for 900 seconds. The assembly was

then cooled back to room temperature ($\sim 25\text{ }^{\circ}\text{C}$), and the pressure was slowly removed from the device.

Once several devices had been imprinted and bonded, the stamp was analyzed using atomic force microscopy (AFM) (Asylum Research MFP-3D Atomic Force Microscope) in repulsive tapping mode at a rate of 0.5 Hz. A Tap300A1-G cantilever tip was used with a force constant of 40 N/m and a frequency of 300kHz. This allowed us to assess the fidelity of the stamp as well as measure the channels being produced. From these scans, it was seen that the pore structures from the bitmap were faithfully transferred not only to the silicon, but also to the resin stamp. The AFM results are shown in Figure 2.10.

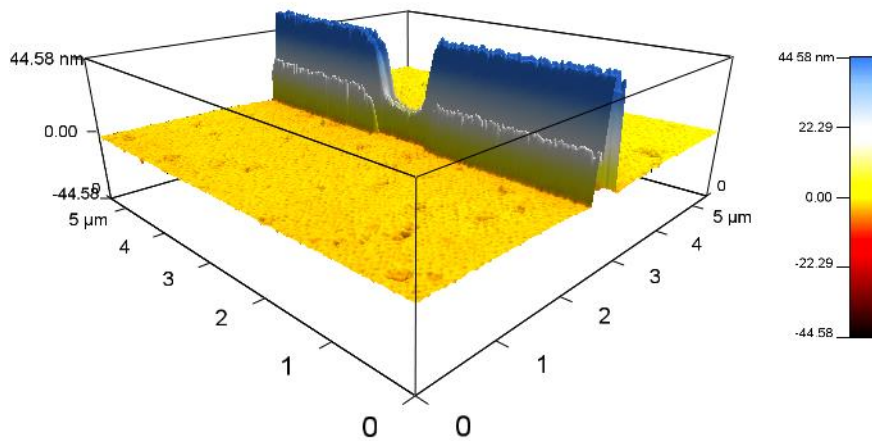


Figure 2.10 Three-dimensionally rendered AFM scan showing the pore structure produced in the resin stamp. This particular stamp had nanochannels 50 nm deep with a 10 nm deep nanopore. This image was captured on an Asylum Research MFP-3D Atomic Force Microscope in repulsive tapping mode at a rate of 0.5 Hz. A Tap300A1-G cantilever tip was used with a force constant of 40 N/m and a frequency of 300kHz.

CHAPTER 3

Integrated Multiscale Module For Diagnostic Applications

3.1 Design Considerations and Requirements

A multiscale device needed to be designed that could carry out multiple solid phase reactions on pillars, have individually addressable subpopulations on those pillars, incorporate the time of flight sensor that was developed in the previous chapter, and allow for re-interrogation to minimize the effects of mis-ligation errors. By incorporating all of this functionality into one chip we can bring in genetic material from the sample, interrogate it with ligase detection reactions and then individually address these pillars by releasing their products into the time-of-flight nanotubes. In order to accomplish this, a multiscale microfluidic module was designed and modeled through an iterative process to create an efficient chip that could accomplish all of the required tasks. More specifically, the chip will be able to:

- 1) Capture poly-T tailed targets using polymer pillars covalently loaded with LDR primers
- 2) Carry out various molecular processing steps on the immobilized targets
- 3) Thermally release solid-phase ligase detection products from the pillar arrays
- 4) Detect and identify single molecules using the time of flight nanosensor developed in the previous chapter

- 5) Perform steps 2-4 multiple times to allow for re-interrogation of the immobilized strands of interest on the pillar arrays

To accomplish all of the tasks required, various chip designs were considered and modeled to understand their behavior. Some of the earlier designs revolved around complex multi-layer devices with vacuum pumps pulling products and waste out in the vertical axis. Another early design explored the idea of individually addressable micro-heaters that would allow for very specific release of spLDR products off of targeted pillars, allowing for products detected to be traced back to a particular location on the chip. However, this design ran into limitations of substrate thickness as well as increasing complexity due to the incredibly abundant heat dissipation channels required to control the flux from the heaters. The design that would turn into the final design presented in this thesis came from the idea of individual pillar array, physically isolated from one another, each with their own single molecule detector. In this way, like in the other designs, the precise location on chip could be known and could be re-interrogated as is required for the particular application.

3.2 Final Design

After an iterative design process that will be discussed further later, a final design was developed that fulfills all off the design constraints and capabilities previously outlined. An overview of this design can be seen in Figure 3.1.

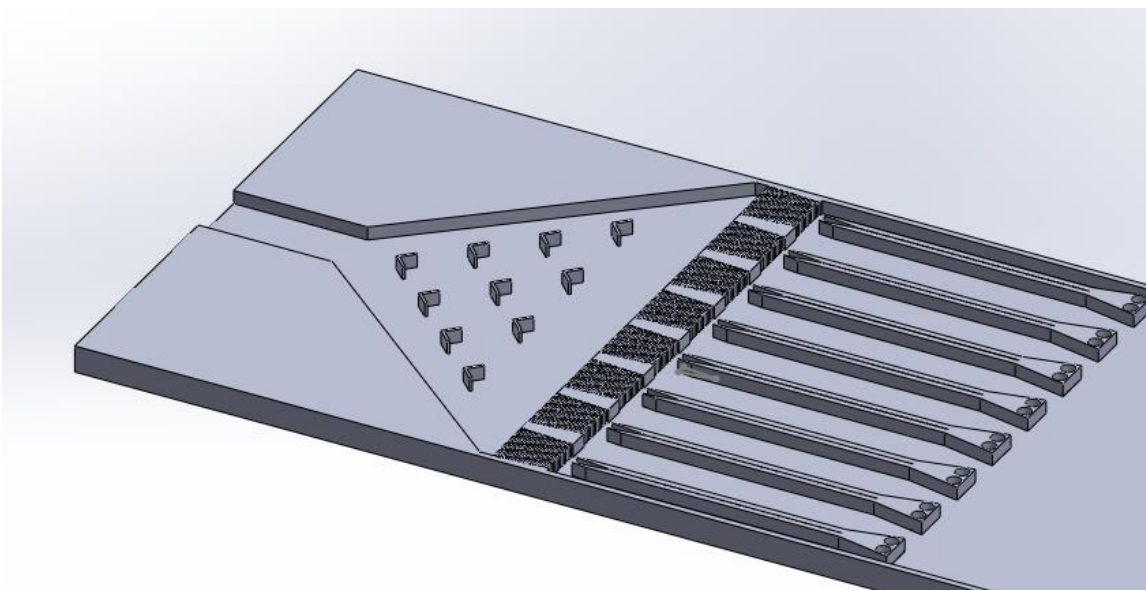


Figure 3.1 Overview of the final chip design ($410\mu\text{m} \times 200\mu\text{m}$). More details and structures labeled in Figure 3.10.

As can be seen in the final design, 8 nanosensors are placed in parallel within a single chip. Each nanosensor has its own pillar “reaction bed” on which ligase detection reactions can take place to identify and capture target biomarkers. All of the important functionality of this chip will be discussed.

An important breakthrough that allowed this design to be feasible was the notion of a hybrid drive system for the chip. In this hybrid system, all of the initial genetic material for analysis is loaded on to the chip with hydrodynamic flow. Then, once the target molecules have attached to the pillar arrays, the waste is pumped off hydrodynamically. Finally, once the products are alone in the chip on the pillars, they are released and driven electrophoretically into the nano time of flight tubes. This novel scheme allowed for the pillars to be located so close together and for the flight tubes to not get clogged with debris (discussed later in this chapter).

Once this final device was created in SolidWorks 2013, it was imported into COMSOL so that important functions could be modeled and understood (COMSOL was used at each design step as a way to verify). The first simulation that was looked at was simply the hydrodynamic flow profile through the chip, essentially, how would fluid move during the loading and waste removal stages. The resulting flow profile can be seen in Figure 3.2.

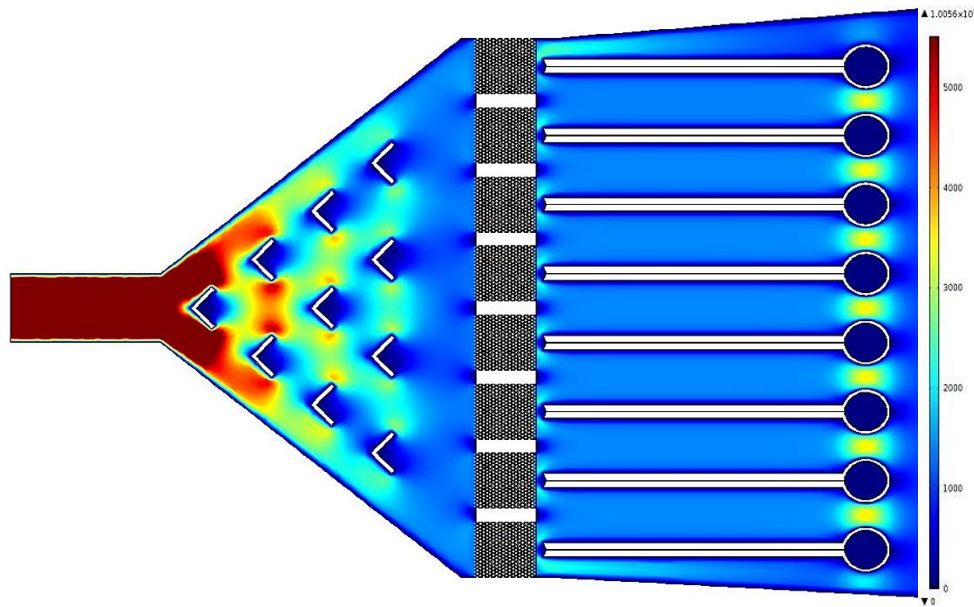


Figure 3.2 Steady-state hydrodynamic flow profile through the entire chip resulting from an input of 1 nL/s (velocity scale is $\mu\text{m/s}$). As a 2D model, several assumptions were made including a thin film assumption and a no-slip condition at the wall. A fine mesh was used.

Next, we focused in on the regions that are critical to the device functioning. Figure 3.3 shows that flow is uniform through the pillars and that the hydrodynamic resistance of the nano flight tube is approaching infinity so that no material will enter the tube when the chip is being actuated via hydrodynamic flow. The exact capture efficiency of the pillar array will depend on the length of the particles being flowed through the reactor, but the uniform pressure drop indicates uniform capture distribution across the array.

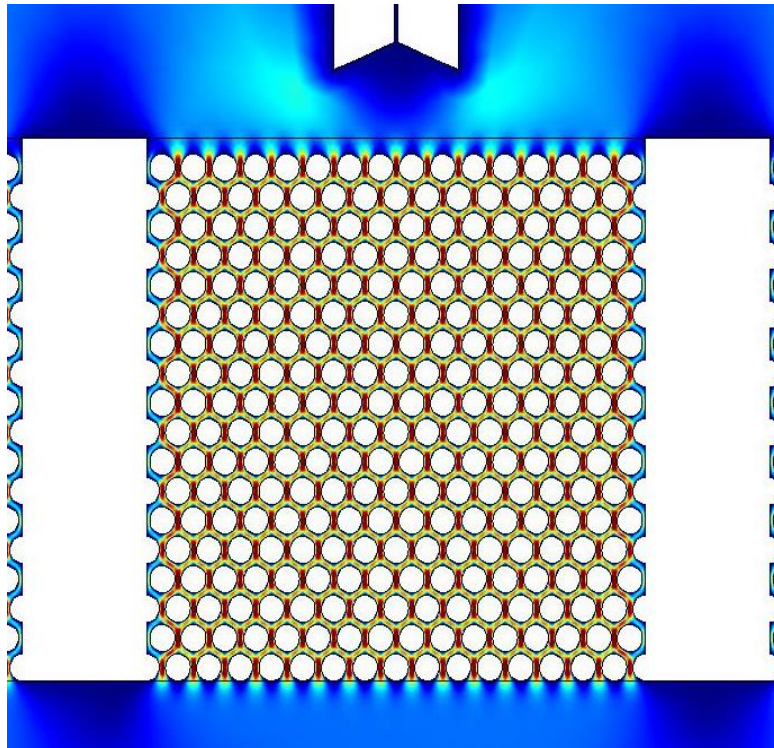


Figure 3.3 Hydrodynamic flow profile at the critical elements of the chip. Again, a 1 nL/s input flow was used and the velocity scale is in $\mu\text{m/s}$. With this flow rate the linear velocity averages $6000 \mu\text{m/s}$ through the pillars which yields approximately a 74.5% capture probability.

The next experiment performed on this design in COMSOL evaluated the Chevron baffles placed at the entrance. As can be seen in Figure 4.5, these chevrons do a good job of splitting the flow into five streams spaced across the width of the chip, rather than a single stream moving straight through the middle. However, the flow profile is not nearly as interesting as the particle trajectories when they meet the chevrons. The intent of the chevrons is to split the flow in such a way that each pillar array has an equal chance of receiving particles. In this way not only the center arrays will receive samples, we want to make sure the entire surface area of the pillar arrays is utilized as much as possible. A movie was generated from this simulation, showing the particles in motion, however, the still image of the trajectories tells the story well enough, Figure 3.4.

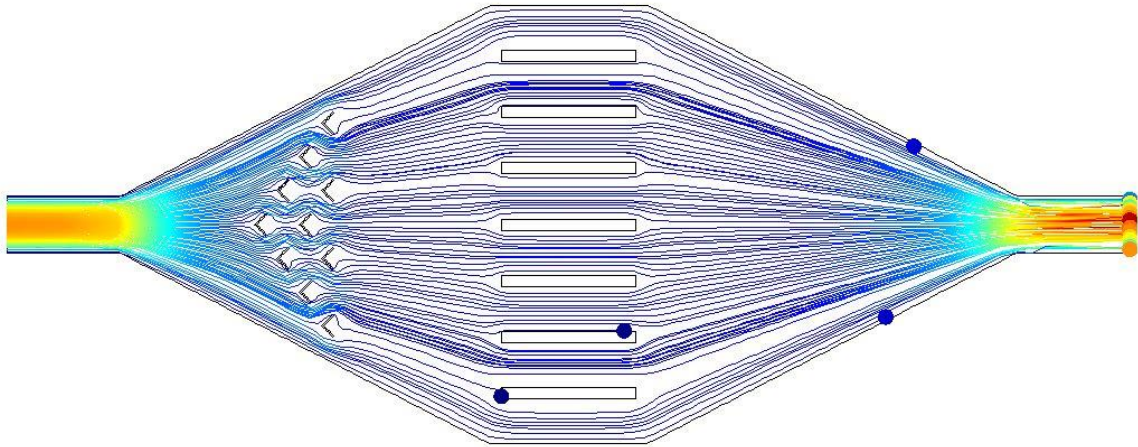


Figure 3.4 Particle traces through second generation design device taken from a video of the particles moving through the chip. 100 particles were introduced in this simulation, and between 9 and 14 entered into each “bay”, indicating that the chevrons were effective at evenly separating the particles shortly after the input.

The final simulation involved the offloading of product from the pillars into the flight tubes for analysis. In these experiments no hydrodynamic pumping was occurring, only the electrokinetic movement generated by the potential applied at the entrance to the chip with ground connections at the reservoir of each individual nano flight tube. Figures 3.5 shows the electric field across the entire chip. Figure 3.6 shows the electric field only at the critical areas, indicating that when the electric field is turned on, all biomarker targets released from the pillar arrays will flow into the detection tubes and not out into waste beyond the sensors. The importance of this feature cannot be overstated. When working with extremely rare molecules, single counts can make a difference.

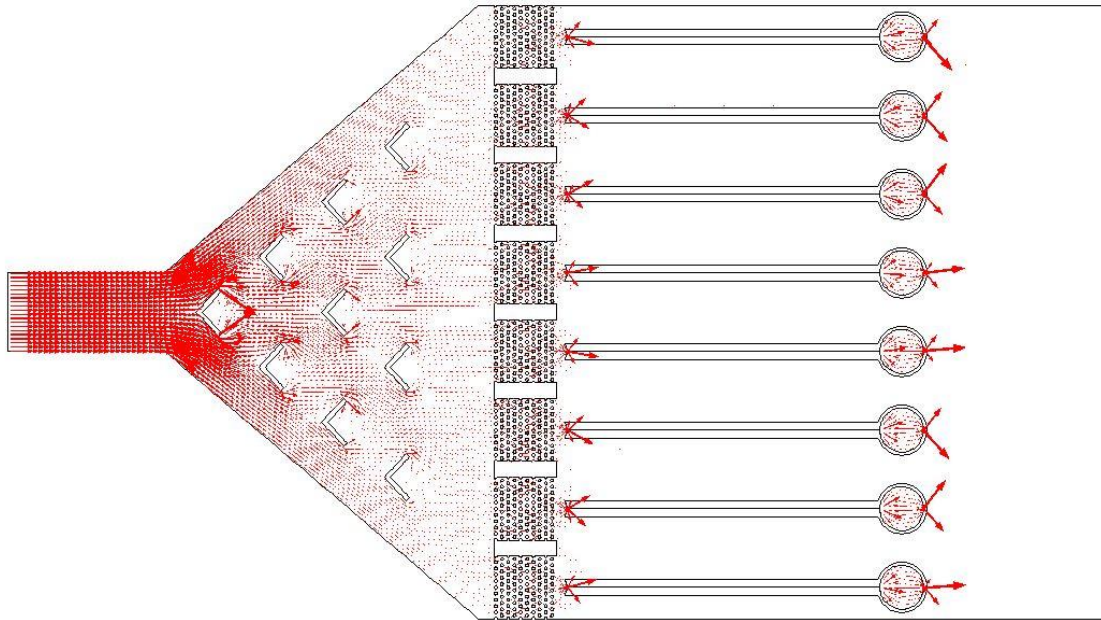


Figure 3.5 Electric field across entire chip, strength is proportional to arrow magnitude. This was created by placing a 10V potential being applied in the entrance to the chip with individual grounds at the end of each nanosensor flight-tube.

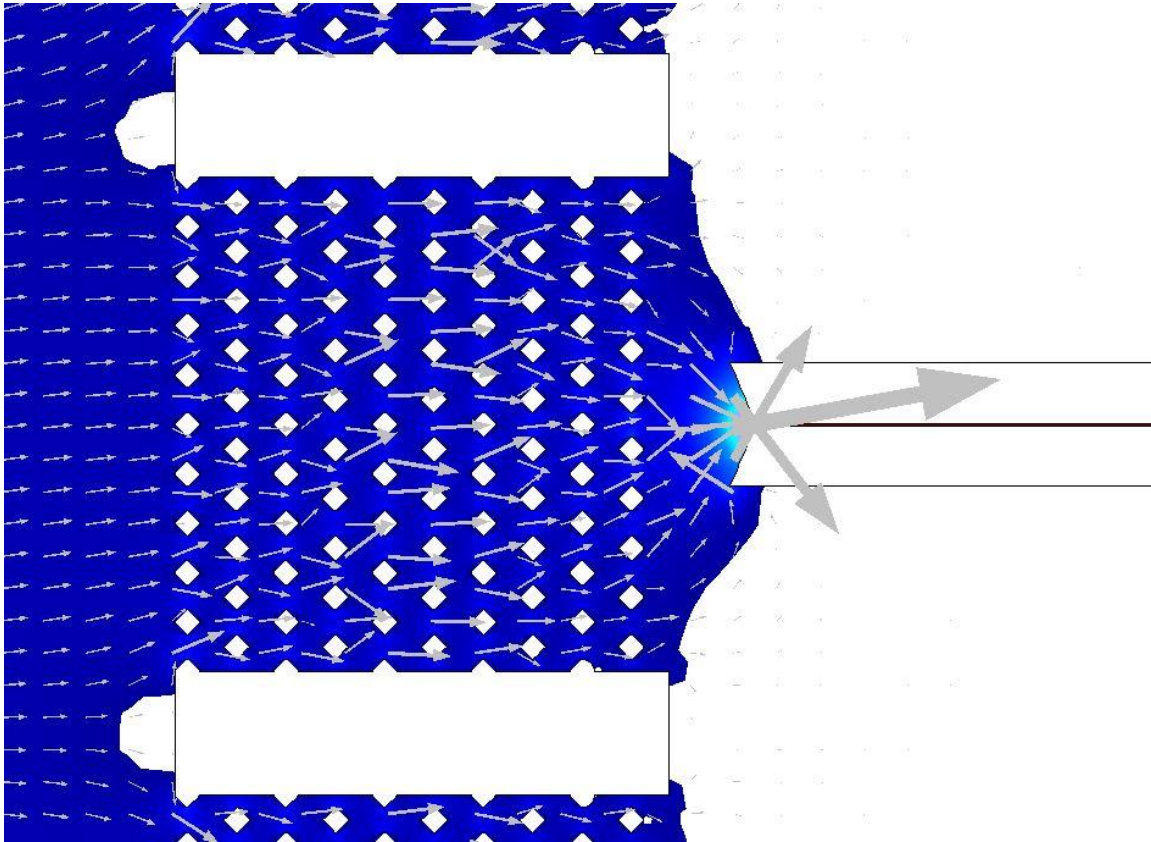


Figure 3.6 Electric field lines at the critical area of the detection chip. All arrows are converging into the flight tube, creating an electrical boundary between individual pixels and flight-tubes. This design should minimize any chance of cross-talk between the sensors.

3.3 An Iterative Design Process

Initial designs varied greatly and looked markedly different from the final design that was presented, suggesting the power of an iterative process to optimize a design application. Successful design elements from early models were combined, largely with the assistance of COMSOL, as a tool to simulate these early designs and understand their flaws. One such early design utilized offset spacing of pillars, input

and outputs in four directions, and individually addressable heaters. An example of one such design can be seen in Figure 3.7.

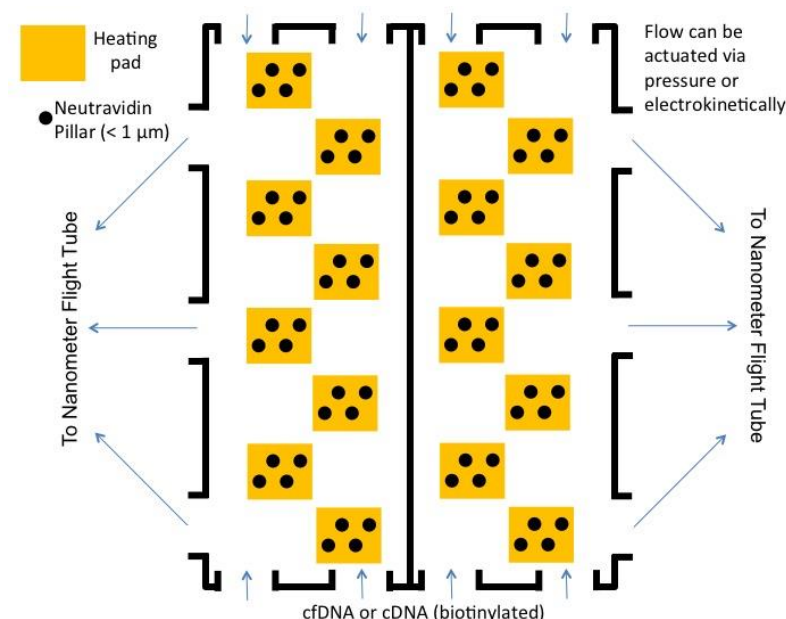


Figure 3.7 Earliest design of multiscale device.

During the modeling of this design, it was quickly realized that the design was too complicated to be reproducible and scalable, the inputs and outputs from multiple directions would have required much more external equipment and the heater placement would have required multi-level channels with precise alignment. As was already discussed, the individually addressed heaters in close proximity had insurmountable challenges to a functional device. An example of this heat flux problem can be seen in Figure 3.8, the values associated with the heat waves are not as important as the fact that they propagate despite the thermal isolation grooves built into the chip design. In an ideal solution the heat waves would start at the

center of the middle pillar array and terminate at the isolation grooves on either side, allowing for precise release off of each individual pillar array. This was simply not possible in the thermoplastics that we were interested in using for this application.

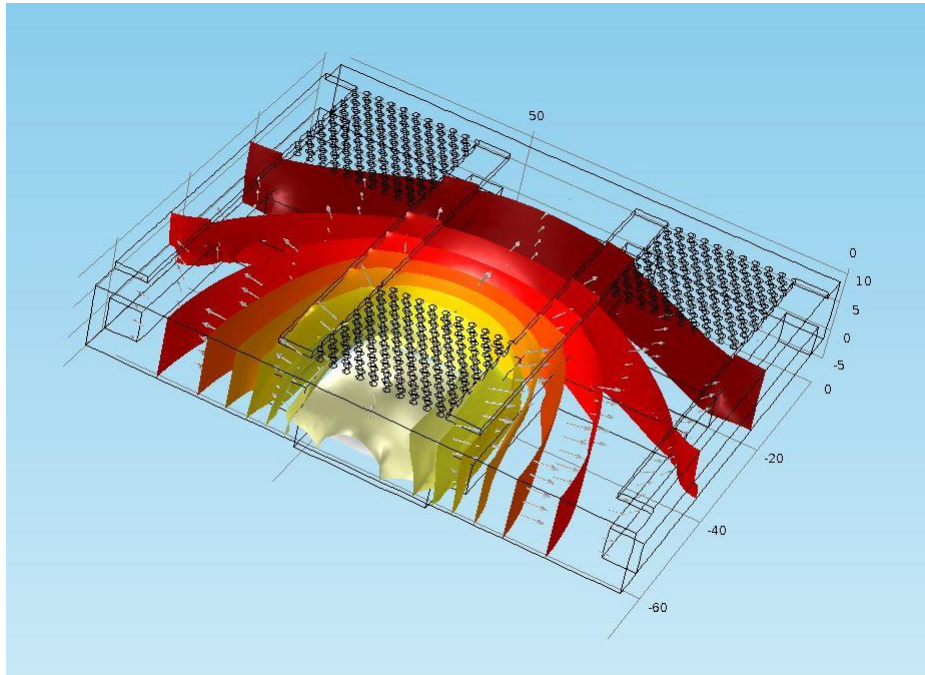


Figure 3.8 Heat model of individually addressable heater with thermal isolation grooves. This illustrates the challenge that despite including many heat mitigation and isolation techniques (see grooves and staggering), the heater beneath each pixel simply radiated too much heat to the surrounding pixels, making precise control of the thermal release impossible.

Building from this knowledge set secured from previous designs, a new device architecture was developed that addresses operational issues evident from previous renditions. For example, the flow was simplified to move in only one direction. However, individually addressable heaters were still being considered. In

this type of design, multiple pillar arrays shared 1 detector. An example can be seen in Figure 3.9.

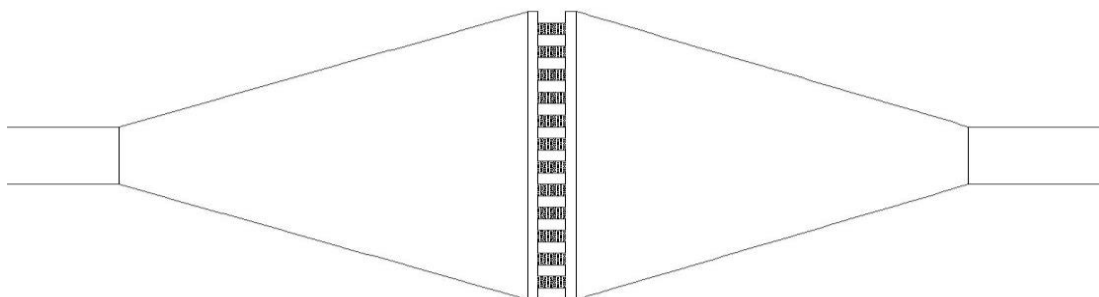


Figure 3.9 Second generation design with unidirectional flow and individual heaters. This design was a “stepping stone” to the ideas present in the final design and was not simulated extensively.

Second generation designs were modeled extensively, and had a lot of really nice properties, however, the individually addressable heaters remained the failing point, with thermal isolation being impossible if enough heat was going to make it through the substrate to interact with the molecules attached to the pillar arrays. The third generation built upon these designs and incorporated some new elements as well. These devices will be configured with a number of fluidic chambers that are comprised of Chevron baffles to allow uniform addressing of 8 pixels ($20 \times 20 \mu\text{m}$; $1 \mu\text{m} \times 5 \mu\text{m}$ pillars; 288 pillars per pixel) and a nanochannel flight tube situated at the output end of each pixel (as described in Chapter 2). As shown and discussed previously, the basic final design can be seen in Figure 3.10.

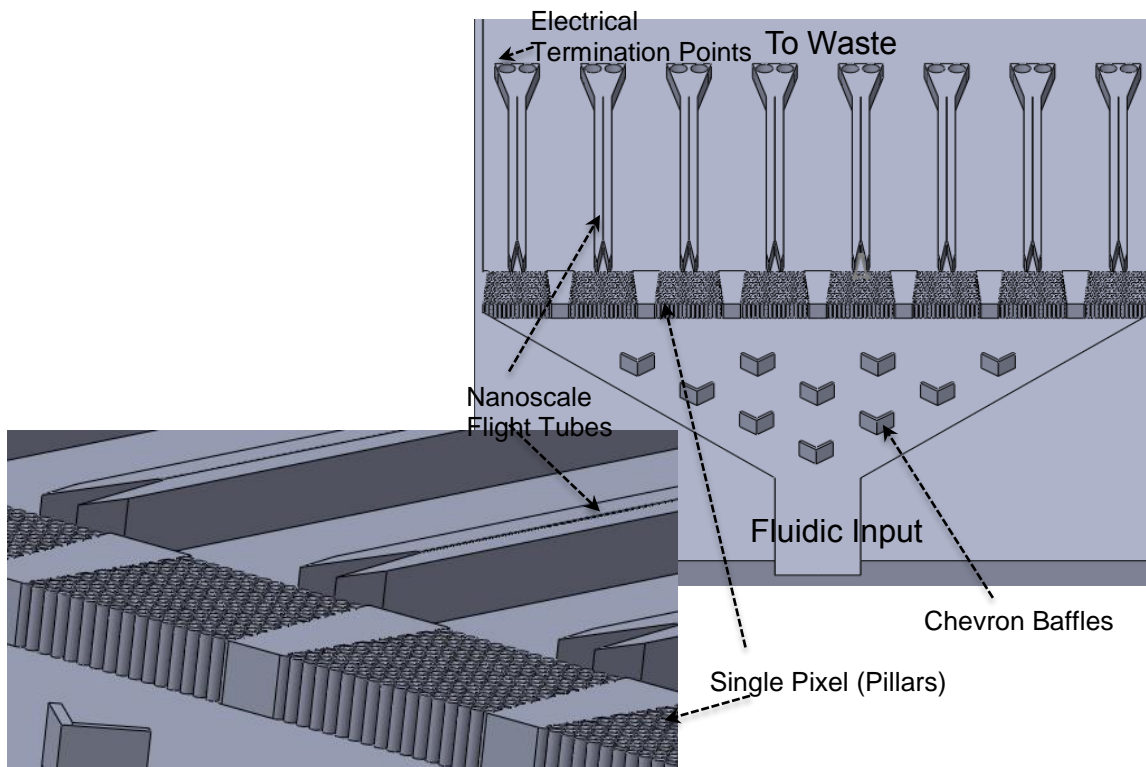


Figure 3.10 Final device design, looking from the entrance down the module as well as a zoomed in view with important features labeled. This design incorporates many of the elements from the previous designs.

This chapter illustrates the design path that was taken to fulfill the design parameters given to me by my lab group for the chip’s use in the modular molecular processing device. By using an iterative process all of the best attributes from each design were included in future designs while detrimental elements were excluded. This design will likely need to be fine-tuned further to the individual requirements necessary for unique diagnostic applications. However, the basic design will be extremely flexible and useful for many applications. By utilizing a straight-through flow (1 input, 1 output), this can be placed in series in any fluidic circuit. The individually addressable flight tubes and “dual-mode” drive allow for very precise measurements with very little risk of contamination or fouling from waste.

CHAPTER 4

Conclusion

This thesis outlines the work done for my master's project. This project combined engineering, chemistry, and some biology in order to understand the design requirements for these two critical components of the universal molecular processing system that Dr. Soper's research group is working on creating.

The time-of-flight sensor that was designed utilizes two nanopores in series to create two regions of resistive pulse sensing. This design scheme should give excellent sensitivity by leveraging three distinct measurements while mitigating a lot of potential disadvantages from co-residence issues and fabrication difficulty. COMSOL simulations were utilized to guide our design and optimize the parameters of the sensor, allowing us to iterate over many variables without wasting resources on fabricating failed devices. These experiments were included in this report to demonstrate the design process.

The integrated multiscale module built upon the time of flight sensor we designed and added in the previous processing step as well as the modality for isolating and controlling what flows into the sensor. By utilizing multiple sensors on one module we were also able to make this system re-addressable, helping to deal with the problem of mis-ligation events when working with ligating enzymes. This chip was also designed to work under two flow conditions. The first is a

hydrodynamic flow, which loads the pillars, carries out the reaction, and then removes the waste. The second flow profile is the electrokinetic, which drives the ligation products into the time-of-flight sensors for analysis.

Some fabrication was completed on a proof-of-concept time-of-flight sensor; however, fabrication will be the main next steps for these devices. Despite following fabrication strategies used in other areas of our work, there will certainly be challenges associated with fabricating these devices. Fortunately, these devices can be easily made on different length scales and still function, so some fabrication issues may be avoided simply by scaling the devices correctly for specific applications.

REFERENCES

- (1) Yager, P.; Edwards, T.; Fu, E.; Helton, K.; Nelson, K.; Tam, M. R.; Weigl, B. H. *Nature* **2006**, *442*, 412–418.
- (2) Feigin, V. L.; Lawes, C. M.; Bennett, D. a.; Barker-Collo, S. L.; Parag, V. *Lancet Neurol.* **2009**, *8*, 355–369.
- (3) Norris, J. W.; Hachinski, V. C. *Lancet* **1982**, *1*, 328–331.
- (4) Goldstein, L. B. *Stroke* **2005**, *293*, 2391–2402.
- (5) Baird, a E. *Biochem. Soc. Trans.* **2006**, *34*, 1313–1317.
- (6) Pullagurla, S. R.; Witek, M. A.; Jackson, J. M.; Lindell, M. A. M.; Hupert, M. L.; Nesterova, I. V; Baird, A. E.; Soper, S. A. *Anal. Chem.* **2014**, *86*, 4058–4065.
- (7) Moerner, W. E.; Ambrose, W. P. *Phys. Rev. Lett.* **1991**, *66*, 1376.
- (8) Brooks Shera, E.; Seitzinger, N. K.; Davis, L. M.; Keller, R. A.; Soper, S. A. *Chem. Phys. Lett.* **1990**, *174*, 553–557.
- (9) Trautman, J. K.; Macklin, J. J.; Brus, L. E.; Betzig, E. *Nature* **1994**, *369*, 40–42.
- (10) Funatsu, T.; Harada, Y.; Tokunaga, M.; Saito, K.; Yanagida, T. Imaging of single fluorescent molecules and individual ATP turnovers by single myosin molecules in aqueous solution. *Nature*, 1995, *374*, 555–559.
- (11) Ishii, Y.; Yanagida, T. *Single Mol.* **2000**, *1*, 5–16.
- (12) Zander, C.; Drexhage, K. H.; Han, K.-T.; Wolfrum, J.; Sauer, M. *Chem. Phys. Lett.* **1998**, *286*, 457–465.
- (13) Lyon, W. a; Nie, S. M. *Anal. Chem.* **1997**, *69*, 3400–3405.
- (14) Dickson RM, Norris DJ, TzengYL, M. W. *Science (80-.).* **1996**, *8*.
- (15) Information, S.; Emory, J. M.; Peng, Z.; Young, B.; Hupert, M. L.; Rousselet, A.; Patterson, D.; Ellison, B.; Soper, S. A.; Rouge, B. **2011**.
- (16) Holland, C. a.; Kiechle, F. L. *Curr. Opin. Microbiol.* **2005**, *8*, 504–509.
- (17) Fan, Y.; Chen, X. T.; Tung, C. H.; Kong, J. M.; Gao, Z. Q. *TRANSDUCERS EUROSENSORS '07 - 4th Int. Conf. Solid-State Sensors, Actuators Microsystems* **2007**, 1887–1890.

- (18) Yi, M.; Jeong, K. H.; Lee, L. P. *Biosens. Bioelectron.* **2005**, *20*, 1320–1326.
- (19) Cui, Y.; Wei, Q.; Park, H.; Lieber, C. M. *Science* **2001**, *293*, 1289–1292.
- (20) Lee, J.; Choi, Y.; Pio, M.; Seo, J.; Lee, L. *MRS Proc.* **2002**, *729*.
- (21) Oh, S.; Lee, J. S.; Jeong, K. H.; Lee, L. P. *Sixt. Annu. Int. Conf. Micro Electro Mech. Syst. 2003. MEMS-03 Kyoto. IEEE* **2003**, 52–55.
- (22) Coulter, W. H. Means for Counting Particles Suspended in a Fluid, 1953.
- (23) Graham, M. D. *JALA - J. Assoc. Lab. Autom.* **2003**, *8*, 72–81.
- (24) DeBlois, R. W. *Rev. Sci. Instrum.* **1970**, *41*, 909.
- (25) Jagtiani, A. V.; Zhe, J.; Hu, J.; Carletta, J. *Meas. Sci. Technol.* **2006**, *17*, 1706–1714.
- (26) Zhang, H.; Chon, C. H.; Pan, X.; Li, D. *Microfluid. Nanofluidics* **2009**, *7*, 739–749.
- (27) Bayley, H.; Martin, C. R. *Chem. Rev.* **2000**, *100*, 2575–2594.
- (28) Saleh, O. a.; Sohn, L. L. *Rev. Sci. Instrum.* **2001**, *72*, 4449–4451.
- (29) Zhang, Z.; Zhe, J.; Chandra, S.; Hu, J. *Atmos. Environ.* **2005**, *39*, 5446–5453.
- (30) Braha, O.; Gu, L. Q.; Zhou, L.; Lu, X.; Cheley, S.; Bayley, H. *Nat. Biotechnol.* **2000**, *18*, 1005–1007.
- (31) DeBlois, R. W.; Wesley, R. K. *J. Virol.* **1977**, *23*, 227–233.
- (32) Kasianowicz, J. J.; Brandin, E.; Branton, D.; Deamer, D. W. *Proc. Natl. Acad. Sci. U. S. A.* **1996**, *93*, 13770–13773.
- (33) Saleh, O. a.; Sohn, L. L. *Proc. Natl. Acad. Sci. U. S. A.* **2003**, *100*, 820–824.
- (34) Tsao, C. W.; DeVoe, D. L. *Microfluid. Nanofluidics* **2009**, *6*, 1–16.
- (35) Ren, K.; Zhou, J.; Wu, H. *Acc. Chem. Res.* **2013**, *XXX*, 130611100147001.
- (36) Piruska, A.; Nikcevic, I.; Lee, S. H.; Ahn, C.; Heineman, W. R.; Limbach, P. a; Seliskar, C. J. *Lab Chip* **2005**, *5*, 1348–1354.
- (37) Tsao, C. W.; Hromada, L.; Liu, J.; Kumar, P.; DeVoe, D. L. *Lab Chip* **2007**, *7*, 499–505.

- (38) Chantiwas, R.; Hupert, M. L.; Pullagurla, S. R.; Balamurugan, S.; Tamarit-López, J.; Park, S.; Datta, P.; Goettert, J.; Cho, Y.-K.; Soper, S. a. *Lab Chip* **2010**, *10*, 3255–3264.
- (39) Ogończyk, D.; Wegrzyn, J.; Jankowski, P.; Dabrowski, B.; Garstecki, P. *Lab Chip* **2010**, *10*, 1324–1327.
- (40) Soper, S. a.; Henry, A. C.; Vaidya, B.; Galloway, M.; Wabuyele, M.; McCarley, R. L. *Anal. Chim. Acta* **2002**, *470*, 87–99.
- (41) Roy, S.; Yue, C. Y.; Lam, Y. C.; Wang, Z. Y.; Hu, H. *Sensors Actuators B Chem.* **2010**, *150*, 537–549.
- (42) Rohr, T.; Ogletree, D. F.; Svec, F.; Fréchet, J. M. J. *Adv. Funct. Mater.* **2003**, *13*, 264–270.
- (43) Khanarian, G.; Celanese, H. *Opt. Eng.* **2001**, *40*, 1024.
- (44) Mao, X.; Huang, T. J. *Lab Chip* **2012**, *12*, 1412.
- (45) Peng, Z.; Young, B.; Baird, A.; Soper, S. *Anal. Chem.* **2013**, *85*, 7851–7858.
- (46) Soper, S. a.; Brown, K.; Ellington, A.; Frazier, B.; Garcia-Manero, G.; Gau, V.; Gutman, S. I.; Hayes, D. F.; Korte, B.; Landers, J. L.; Larson, D.; Ligler, F.; Majumdar, A.; Mascini, M.; Nolte, D.; Rosenzweig, Z.; Wang, J.; Wilson, D. *Biosens. Bioelectron.* **2006**, *21*, 1932–1942.
- (47) Adams, A. a.; Okagbare, P. I.; Feng, J.; Hupert, M. L.; Patterson, D.; Göttert, J.; McCarley, R. L.; Nikitopoulos, D.; Murphy, M. C.; Soper, S. a. *J. Am. Chem. Soc.* **2008**, *130*, 8633–8641.
- (48) Chen, X.; Ba, Y.; Ma, L.; Cai, X.; Yin, Y.; Wang, K.; Guo, J.; Zhang, Y.; Chen, J.; Guo, X.; Li, Q.; Li, X.; Wang, W.; Zhang, Y.; Wang, J.; Jiang, X.; Xiang, Y.; Xu, C.; Zheng, P.; Zhang, J.; Li, R.; Zhang, H.; Shang, X.; Gong, T.; Ning, G.; Wang, J.; Zen, K.; Zhang, J.; Zhang, C.-Y. *Cell Res.* **2008**, *18*, 997–1006.
- (49) Han, J.; Craighead, H. G. *Proc. SPIE* **2000**, *4177*, 11–17.
- (50) Sharma, R.; Laskowitz, D. T. *Curr. Neurol. Neurosci. Rep.* **2012**, *12*, 560–569.
- (51) Jeter, C. B.; Hergenroeder, G. W.; Hylin, M. J.; Redell, J. B.; Moore, A. N.; Dash, P. K. *J. Neurotrauma* **2013**, *30*, 657–670.
- (52) Peng, Z. Single Molecule Detection of Molecular Beacons Generated from LDR on Thermoplastic Microfluidic Device for Bioanalysis, Louisiana State University, 2012.

- (53) Emory, J. M.; Peng, Z.; Young, B.; Hupert, M. L.; Rousselet, A.; Patterson, D.; Ellison, B.; Soper, S. a. *Analyst* **2012**, *137*, 87–97.
- (54) Harms, Z. D.; Haywood, D. G.; Kneller, A. R.; Selzer, L.; Zlotnick, A.; Jacobson, S. C. **2014**.
- (55) Uba, F. I.; Pullagurla, S. R.; Sirasunthorn, N.; Wu, J.; Park, S.; Chantiwas, R.; Cho, Y.-K.; Shin, H.; Soper, S. a. *Analyst* **2015**, *140*, 113–126.
- (56) Uba, F. I.; Hu, B.; Weerakoon-Ratnayake, K.; Oliver-Calixte, N.; Soper, S. a. *Lab Chip* **2014**.